
Architecture–Optimization Co-Design for Physics-Informed Neural Networks Via Attentive Representations and Conflict-Resolved Gradients

Pancheng Niu

College of Applied Mathematics
Chengdu University of Information Technology
Chengdu 610225, Sichuan, China

Jun Guo*

College of Applied Mathematics
Chengdu University of Information Technology
Chengdu 610225, Sichuan, China

Qiaolin He

College of Mathematics
Sichuan University
Chengdu 610064, Sichuan, China

Yongming Chen

College of Applied Mathematics
Chengdu University of Information Technology
Chengdu 610225, Sichuan, China

Yanchao Shi

School of Sciences
Southwest Petroleum University
Chengdu 610500, Sichuan, China

ABSTRACT

Physics-Informed Neural Networks (PINNs) provide a learning-based framework for solving partial differential equations (PDEs) by embedding governing physical laws into neural network training. In practice, however, their performance is often hindered by limited representational capacity and optimization difficulties caused by competing physical constraints and conflicting gradients. In this work, we study PINN training from a unified architecture-optimization perspective. We first propose a layer-wise dynamic attention mechanism to enhance representational flexibility, resulting in the Layer-wise Dynamic Attention PINN (LDA-PINN). We then reformulate PINN training as a multi-task learning problem and introduce a conflict-resolved gradient update strategy to alleviate gradient interference, leading to the Gradient-Conflict-Resolved PINN (GC-PINN). By integrating these two components, we develop the Architecture-Conflict-Resolved PINN (ACR-PINN), which combines attentive representations with conflict-aware optimization while preserving the standard PINN loss formulation. Extensive experiments on benchmark PDEs, including the Burgers, Helmholtz, Klein-Gordon, and lid-driven cavity flow problems, demonstrate that ACR-PINN achieves faster convergence and significantly lower relative L_2 and L_∞ errors than standard PINNs. These results highlight the effectiveness of architecture-optimization co-design for improving the robustness and accuracy of PINN-based solvers.

Keywords Physics-informed neural networks; Partial differential equations; Multi-task learning; Attention mechanisms; Gradient-based optimization; Scientific machine learning

1 Introduction

Physics-informed neural networks (PINNs) provide a unified computational framework for solving partial differential equations (PDEs) by directly incorporating governing physical laws into the neural network training process [1, 2]. In this framework, the residuals of the underlying PDEs, along with initial and boundary conditions, are imposed as soft

*Correspondence: junguo0407@cuit.edu.cn

constraints through a single composite loss function. The use of automatic differentiation enables accurate evaluation of differential operators without explicit discretization, allowing PINNs to represent solutions in a mesh-free manner and to address both forward and inverse problems within the same optimization setting [3]. However, subsequent studies have shown that the training behavior of PINNs can be highly sensitive and problem-dependent [4]. Due to these characteristics, PINNs have been explored in a variety of scientific and engineering contexts, including fluid dynamics [5, 6], heat transfer [7, 8], solid mechanics [9, 10], wave propagation phenomena such as acoustic and elastic waves [11, 12], and complex periodic water waves [13].

Despite these advances, the practical training of PINNs remains a significant challenge, especially for problems characterized by strong nonlinearity, multiscale dynamics, or multiple competing physical constraints. Conventional PINN formulations often exhibit slow or unstable convergence, pronounced sensitivity to hyperparameter selection, and a tendency to converge to inaccurate or biased solutions. Importantly, these limitations cannot be solely attributed to numerical discretization errors; rather, they stem from complex interactions between the neural network's expressive capacity and the optimization dynamics governing the training process [14, 15]. Recent studies have further demonstrated that optimization behavior and the conditioning of the loss landscape play a pivotal role in determining PINN convergence and stability [16, 17]. Moreover, without tailored architectural designs or algorithmic interventions, standard PINNs often struggle to handle steep gradients, multiscale solution features, and imbalanced residual contributions [18].

A growing body of recent studies has aimed to enhance the performance of PINNs through multiple complementary approaches. From an optimization perspective, substantial efforts have been devoted to improving training dynamics and the conditioning of the loss landscape. Representative approaches include adaptive loss weighting schemes [14, 19, 20, 21], gradient-enhanced formulations [22, 23], minimax or dual optimization frameworks [24], as well as analyses and training strategies inspired by neural tangent kernels [15] and loss/optimization landscape diagnostics [25]. In parallel, various architectural modifications have been proposed to enhance the representational capacity of PINNs, including attention-based network designs [14], adaptive activation functions [26], Fourier feature embeddings [27], and Kolmogorov–Arnold networks [28]. These methods aim to mitigate spectral bias and enhance the ability of neural networks to capture multiscale or highly oscillatory solution structures. Despite the demonstrated effectiveness of these advances, most existing approaches are still developed in a largely decoupled manner, implicitly treating network representation and optimization strategy as independent design choices. As a result, improvements in expressivity or optimization stability are often pursued independently, without explicitly considering their combined effects on gradient interactions and the overall training dynamics in PINNs.

A key observation is that the coupling between architecture and optimization becomes explicit when PINN training is analyzed through the structure of its composite loss function. Standard PINNs minimize a weighted objective function that aggregates multiple heterogeneous physical constraints, including PDE residuals, boundary conditions, and initial conditions. Each constraint contributes a distinct loss term and an associated gradient component. The interaction among these task gradients plays a central role in determining convergence behavior and training stability. Recent studies have shown that gradients induced by various physical constraints can exhibit significant imbalances or even directional conflicts, resulting in inefficient or unstable optimization [22, 29, 14]. Importantly, the geometry of these gradients is not fixed. It is shaped by the underlying network representation, which governs how physical information is encoded and propagated throughout the model. The optimization algorithm determines how competing gradient signals are balanced and reconciled during training. From this perspective, effectively addressing gradient conflicts in PINNs requires a combined approach that considers both network architecture and optimization strategy, rather than improving each component in isolation.

Motivated by these observations, we argue that effective training of PINNs requires a joint consideration of network architecture and optimization strategy, rather than treating them as independent components. Specifically, architectural design influences the distribution, scale, and conditioning of task-specific gradients, while optimization strategies determine how competing gradient signals are balanced and reconciled during training. Neglecting either aspect can fundamentally limit performance: highly expressive architectures may still suffer from unstable or inefficient optimization, while advanced optimization algorithms alone cannot compensate for inherent representational deficiencies.

In this work, we develop a unified *Architecture–Conflict-Resolved Physics-Informed Neural Network* (ACR-PINN) framework that embodies an explicit architecture–optimization co-design philosophy to enable robust PINN training. At the architectural level, inspired by attention-based PINN formulations [14, 21], we propose a *Layer-wise Dynamic Attention* (LDA) framework, in which input coordinates are re-encoded and adaptively modulated at each hidden layer to guide feature construction. By reintroducing coordinate information in a layer-wise, input-conditioned manner, this framework enhances representational flexibility and reshapes gradient propagation throughout the network depth, alleviating excessive gradient concentration and improving training stability. This architectural design naturally leads to the *LDA-PINN* model, which isolates the effect of representation enhancement within the proposed framework. From an optimization perspective and motivated by studies on gradient conflict and task interference in multi-task

learning [22, 29], we reinterpret PINN training as a multi-objective optimization problem. In this context, the PDE residual, initial condition, and boundary condition constraints represent heterogeneous learning tasks that generate competing gradient signals during training. To explicitly address destructive gradient interference among these physical objectives, we introduce a conflict-resolved gradient optimization strategy that operates directly within the gradient space. This strategy gives rise to the *Gradient-Conflict-Resolved PINN* (GC-PINN) model, which isolates the effect of mitigating gradient-level conflicts independently of architectural modifications. By integrating the LDA-based architectural framework with conflict-resolved gradient optimization, ACR-PINN establishes a unified training paradigm in which representation learning and optimization dynamics are jointly coordinated rather than treated independently. This co-design simultaneously mitigates representational deficiencies and optimization instabilities that commonly limit the performance of standard PINNs.

The main contributions of this work are summarized as follows:

- We propose an LDA architecture for PINNs that re-encodes and adaptively modulates input coordinates at each hidden layer through feature-wise gating and residual injection, thereby enhancing representational flexibility. Furthermore, we construct LDA-PINN to isolate and evaluate the architectural contributions.
- We reinterpret PINN training as a multi-task learning problem and provide a gradient-level analysis of intrinsic gradient conflicts induced by heterogeneous physical constraints. Based on this insight, we incorporate conflict-resolved gradient updates and develop GC-PINN to isolate optimization-level conflict mitigation.
- From a coupled architecture-optimization perspective, we analyze the synergy between attentive representations and conflict-resolved optimization, and develop the unified ACR-PINN model by integrating LDA with conflict-resolved gradient updates, while preserving the original PINN loss formulation.
- Extensive numerical experiments on representative PDE benchmarks—including oscillatory Helmholtz equations across varying frequency regimes, nonlinear time-dependent Klein–Gordon equations, and lid-driven cavity flow governed by incompressible Navier–Stokes equations—demonstrate that the proposed models consistently outperform standard PINNs in terms of accuracy, robustness, and convergence behavior.

The remainder of this paper is organized as follows: Section 2 presents the proposed architecture-optimization co-design framework for PINNs. Specifically, we first analyze PINN training from a multi-task gradient perspective and identify the sources of gradient conflicts caused by heterogeneous physical constraints. We then introduce the layer-wise dynamic attention architecture and formulate LDA-PINN to enhance representational flexibility, followed by the conflict-resolved gradient optimization strategy, which leads to the development of GC-PINN. Finally, these two components are integrated into the unified ACR-PINN framework. Section 3 presents comprehensive numerical experiments to evaluate the proposed methods. The test cases include oscillatory Helmholtz equations across varying frequency regimes, nonlinear time-dependent Klein–Gordon equations, and the two-dimensional lid-driven cavity flow governed by the incompressible Navier–Stokes equations. Through systematic comparisons with the standard PINN and its ablation variants, we evaluate accuracy, robustness, and convergence behavior across diverse physical settings. Finally, Section 4 summarizes the main findings of this work and discusses potential directions for future research.

2 Methodology

2.1 Physics-Informed Neural Networks

PINNs constitute a mesh-free learning framework for solving PDEs by embedding the governing physical laws directly into the training objective of neural networks [1]. Rather than relying exclusively on labeled solution data, PINNs utilize automatic differentiation to ensure consistency with the underlying PDEs, as well as the associated initial and boundary conditions. As a result, the learned solution is constrained to satisfy the prescribed physical laws in a weak, optimization-based manner.

Consider a general PDE defined over the spatiotemporal domain $\Omega := \Omega_x \times \Omega_t$,

$$\mathcal{N}[u(x, t)] = 0, \quad (x, t) \in \Omega, \quad (1)$$

where $\mathcal{N}[\cdot]$ denotes a (possibly nonlinear) differential operator characterizing the governing physics. The solution is subject to an initial condition

$$u(x, t_0) = u_0(x), \quad x \in \Omega_x, \quad (2)$$

and a Dirichlet boundary condition

$$u(x, t) = u_b(x, t), \quad (x, t) \in \partial\Omega_x \times \Omega_t, \quad (3)$$

which prescribe the system state at the initial time and along the spatial boundaries, respectively.

Within the PINN framework, the unknown solution $u(x, t)$ is approximated by a neural network $u_\theta(x, t)$ parameterized by θ . This network takes spatiotemporal coordinates as inputs and outputs the corresponding physical quantity of interest. By leveraging automatic differentiation, all derivatives appearing in the operator $\mathcal{N}[\cdot]$ can be accurately evaluated with respect to the network outputs, thereby enabling the direct computation of the PDE residual without explicit discretization.

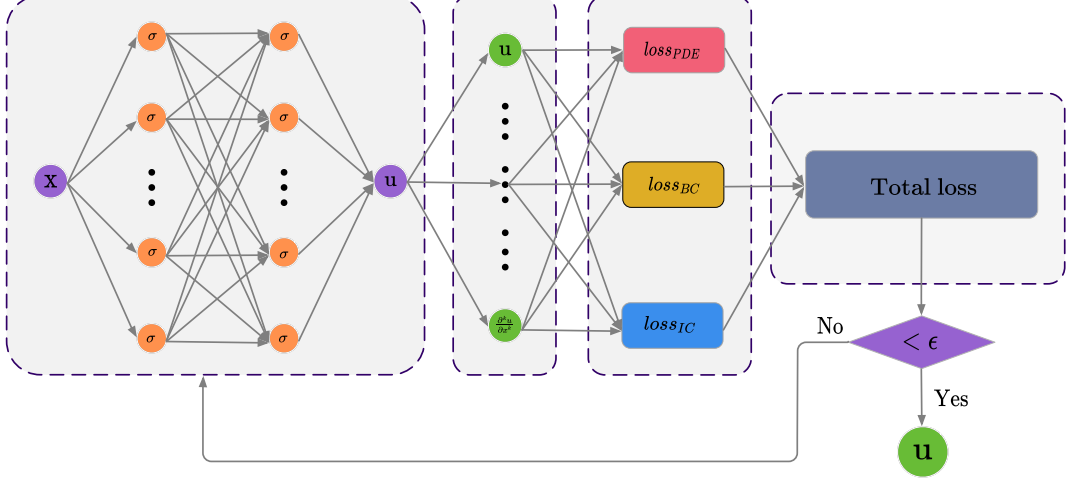


Figure 1: Overall framework of the standard PINN.

As illustrated in Fig. 1, the standard PINN framework enforces physical constraints by minimizing a composite loss function that combines contributions from the PDE residual, the initial conditions, and the boundary conditions.

Specifically, the total training loss is defined as

$$\mathcal{L}(\theta) = \lambda_{\text{PDE}} \mathcal{L}_{\text{PDE}} + \lambda_{\text{IC}} \mathcal{L}_{\text{IC}} + \lambda_{\text{BC}} \mathcal{L}_{\text{BC}}, \quad (4)$$

where \mathcal{L}_{PDE} , \mathcal{L}_{IC} , and \mathcal{L}_{BC} denote the loss terms associated with the PDE residual, the initial condition, and the boundary condition, respectively, and λ_{PDE} , λ_{IC} , λ_{BC} are corresponding weighting coefficients.

These loss components are typically evaluated at a set of collocation points and can be written explicitly as

$$\mathcal{L}_{\text{PDE}} = \frac{1}{N_f} \sum_{i=1}^{N_f} \left| \mathcal{N}[u_\theta(x_f^{(i)}, t_f^{(i)})] \right|^2, \quad (5)$$

$$\mathcal{L}_{\text{IC}} = \frac{1}{N_i} \sum_{i=1}^{N_i} \left| u_\theta(x_i^{(i)}, t_0) - u_0(x_i^{(i)}) \right|^2, \quad (6)$$

$$\mathcal{L}_{\text{BC}} = \frac{1}{N_b} \sum_{i=1}^{N_b} \left| u_\theta(x_b^{(i)}, t_b^{(i)}) - u_b(x_b^{(i)}, t_b^{(i)}) \right|^2. \quad (7)$$

By minimizing the composite loss (4), the network is trained to satisfy the governing equations and associated constraints in a unified optimization framework. Despite their conceptual simplicity and mesh-free formulation, standard PINNs often exhibit limited representational flexibility and suffer from pronounced gradient competition among different loss components, particularly in problems involving multiscale behavior or high-frequency solution features. These limitations motivate the development of enhanced network architectures and more robust optimization strategies, which will be introduced in the following sections.

2.2 Attentive Architecture Design

This subsection presents an attentive architectural design for physics-informed neural networks, incorporating a layer-wise dynamic attention mechanism into a multilayer perceptron (MLP) backbone. The proposed design enables input-conditioned modulation of representations across hidden layers, aiming to enhance the representational flexibility of standard PINNs while maintaining their original training paradigm and numerical stability.

2.2.1 Backbone MLP and Its Limitations

In standard PINNs, MLPs are commonly used as backbone architectures to approximate the mapping from spatiotemporal coordinates to the physical quantities of interest. A standard MLP computes hidden representations recursively as follows:

$$a_\ell = \phi(W_\ell a_{\ell-1} + b_\ell), \quad a_0 = x, \quad (8)$$

where x denotes the input coordinates, W_ℓ and b_ℓ are learnable parameters, and $\phi(\cdot)$ is a nonlinear activation function.

Although multilayer perceptrons are known to possess universal approximation capabilities for continuous functions on compact domains [30], their use within PINNs entails several structural limitations [14]. In standard PINNs, the same input coordinates are implicitly interpreted uniformly across all hidden layers, regardless of the evolving state of the representation. The original input is injected only at the first layer, and its influence on deeper representations is mediated solely through successive nonlinear transformations. As the network depth increases, the direct coupling between hidden features and physical coordinates progressively weakens. This attenuation can impede the modeling of multi-scale solutions, localized sharp gradients, and high-frequency behaviors commonly encountered in PDE problems.

Moreover, standard MLPs lack explicit mechanisms for layer-wise adaptation. Each hidden layer applies a fixed transformation without considering the current hidden state or the heterogeneous physical characteristics across different spatiotemporal regions. As a result, the learned representation remains effectively static across layers, limiting the network's ability to dynamically reinterpret identical physical inputs in different contextual states.

2.2.2 Input Re-encoding via Multiple Views

In standard PINNs, the input coordinates are introduced only at the first layer, and their influence on deeper representations is propagated exclusively through successive nonlinear transformations. As a result, the network lacks an explicit mechanism to condition intermediate features on the physical coordinates at different depths, which can limit its representational flexibility.

However, for partial differential equations characterized by multi-scale structures, strong oscillations, or pronounced nonlinearities, the same physical coordinates may serve different roles at different representational depths. As the network depth increases, the direct coupling between hidden features and the original physical coordinates progressively weakens. This attenuation can limit the model's ability to capture localized sharp gradients, high-frequency components, and complex nonlinear interactions. To overcome this structural limitation, we allow the physical input to be re-encoded at each hidden layer, enabling the network to reinterpret the same coordinates in a manner dependent on the layer.

This layer-wise input re-encoding mechanism offers additional representational degrees of freedom, enabling the model to adapt its interpretation of physical coordinates as feature abstraction progresses through the network's depth. Building on this motivation and inspired by the success of multi-view representation learning and attention mechanisms in deep neural networks [31], as well as recent advances in attention-based designs for physics-informed neural networks [14], we introduce a layer-wise input re-encoding strategy that generates multiple candidate representations of the same physical input at each hidden layer.

Specifically, at layer ℓ , the input coordinates $x \in \mathbb{R}^d$ are independently projected into two distinct feature spaces,

$$e_\ell^{(1)} = \phi(E_\ell^{(1)} x + c_\ell^{(1)}), \quad e_\ell^{(2)} = \phi(E_\ell^{(2)} x + c_\ell^{(2)}), \quad (9)$$

where $E_\ell^{(1)}, E_\ell^{(2)} \in \mathbb{R}^{h_\ell \times d}$ and $c_\ell^{(1)}, c_\ell^{(2)} \in \mathbb{R}^{h_\ell}$ are independently learned parameters at layer ℓ , and h_ℓ denotes the hidden dimension.

These re-encoding branches are not assigned predefined semantic roles. Instead, by employing independent parameterization, they are encouraged to learn complementary representations of the same physical input. Each branch generates a candidate interpretation corresponding to the dimensionality of the current hidden layer, and both views are preserved without applying a fixed combination or fusion rule at this stage. This design explicitly separates input reinterpretation from representation aggregation, delegating the selection and modulation of different views to a subsequent attention mechanism.

2.2.3 Layer-wise Dynamic Gating Mechanism

The central component of the proposed attentive architecture is a layer-wise dynamic gating mechanism that determines how alternative input encodings are utilized at each hidden layer. Let

$$a_\ell^{\text{MLP}} = \phi(W_\ell a_{\ell-1} + b_\ell) \quad (10)$$

denote the intermediate hidden representation produced by the backbone MLP at layer ℓ .

To condition the selection of input representations on the current representation state, the backbone feature and the two input encodings are concatenated to form

$$z_\ell = [a_\ell^{\text{MLP}}; e_\ell^{(1)}; e_\ell^{(2)}] \in \mathbb{R}^{3h_\ell}. \quad (11)$$

The concatenated vector z_ℓ is processed by a lightweight, layer-specific gating network $g_\ell(\cdot)$, implemented as a small multilayer perceptron. This gating network maps \mathbb{R}^{3h_ℓ} to \mathbb{R}^{2h_ℓ} through an intermediate hidden layer, and produces feature-wise gating logits conditioned jointly on the current hidden state and the candidate input encodings.

The output of the gating network is interpreted as a feature-wise gating tensor.

$$G_\ell = g_\ell(z_\ell) \in \mathbb{R}^{2 \times h_\ell}, \quad (12)$$

where the first dimension indexes the two input encoding branches ($i = 1, 2$), and the second dimension corresponds to the feature channels of the current hidden layer ($k = 1, \dots, h_\ell$).

For each feature channel k , a softmax operation is applied across the two encoding branches to obtain normalized gating weights,

$$\alpha_{\ell,k}^{(i)} = \frac{\exp(G_{\ell,i,k})}{\sum_{j=1}^2 \exp(G_{\ell,j,k})}, \quad i = 1, 2, \quad k = 1, \dots, h_\ell. \quad (13)$$

This formulation enables adaptive, feature-wise selection among alternative input representations at each hidden layer, allowing the network to dynamically modulate its interpretation of the original input coordinates based on the evolving state of the representation.

2.2.4 Feature-wise Gated Fusion with Residual Injection

Based on the learned feature-wise gating weights, the encoded input representations are adaptively fused at each hidden layer. Specifically, a modulation term is constructed as

$$m_{\ell,k} = \alpha_{\ell,k}^{(1)} e_{\ell,k}^{(1)} + \alpha_{\ell,k}^{(2)} e_{\ell,k}^{(2)}, \quad k = 1, \dots, h_\ell, \quad (14)$$

where $m_\ell \in \mathbb{R}^{h_\ell}$ denotes the input-conditioned modulation vector at layer ℓ . This gated fusion enables the network to combine alternative input representations in a data-dependent, feature-wise manner.

The modulation term is then incorporated into the backbone representation using a residual formulation.

$$a_\ell = a_\ell^{\text{MLP}} + m_\ell. \quad (15)$$

The residual design ensures that the proposed mechanism enhances, rather than replaces, the original MLP representation. Consequently, the fundamental recursive structure of the backbone network is preserved, while input-conditioned modulation is introduced in a stable and interpretable way.

The overall structure of the proposed LDA mechanism is illustrated in Fig. 2. The left section illustrates the data flow within a single hidden layer, encompassing input re-encoding, feature-wise gating, gated fusion, and residual injection. The right section offers an abstract overview of an MLP enhanced with LDA layers.

From an architectural perspective, the proposed LDA mechanism allows each hidden layer to dynamically reinterpret the original input coordinates based on the current state of the representation. Unlike transformer-style self-attention, the proposed mechanism functions as a gated feature selection process across multiple input representations, rather than modeling pairwise interactions among hidden features.

When embedded within the physics-informed neural network framework, the resulting model is referred to as the LDA-PINN, as illustrated in Fig. 3. Compared to the standard PINN architecture, the only modification in LDA-PINN is in the network backbone, where the conventional MLP is replaced by the proposed LDA-enhanced MLP. All other components, including the formulation of physics-informed loss functions and the training procedure, remain unchanged.

Moreover, the LDA mechanism operates in a layer-wise manner rather than globally, is input-conditioned rather than self-referential, and does not depend on PDE-specific priors. These properties make LDA-PINN broadly applicable across various PINN settings. By enhancing representational flexibility at the architectural level while preserving the original physics-informed learning paradigm, the proposed design offers a more suitable feature space for addressing optimization challenges, which will be discussed in the following section.

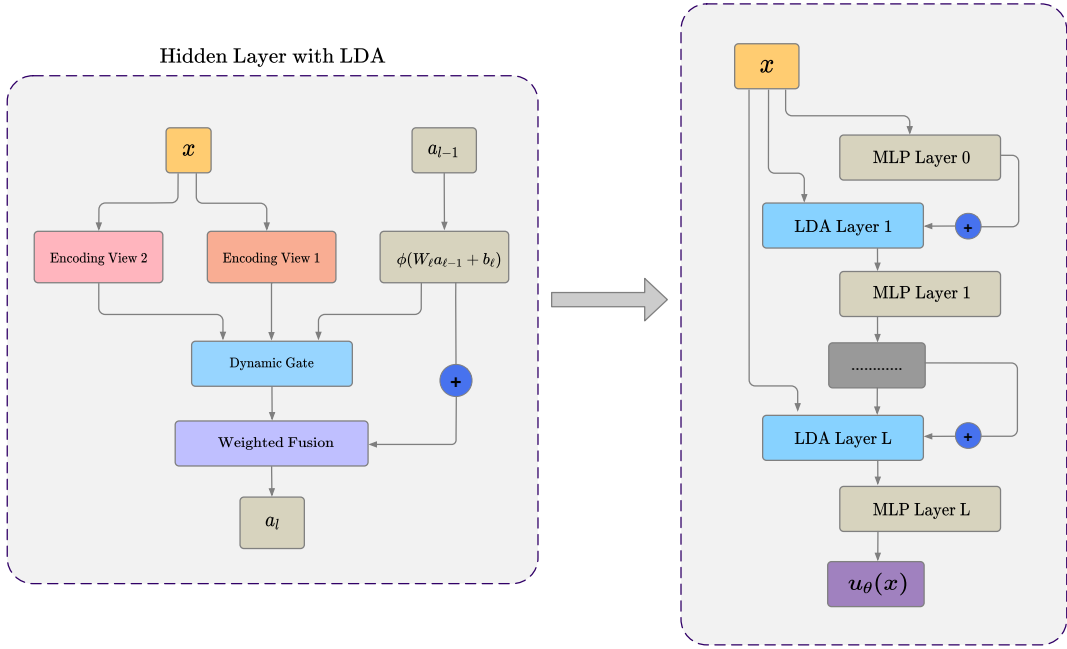


Figure 2: Overall architecture of the LDA module.

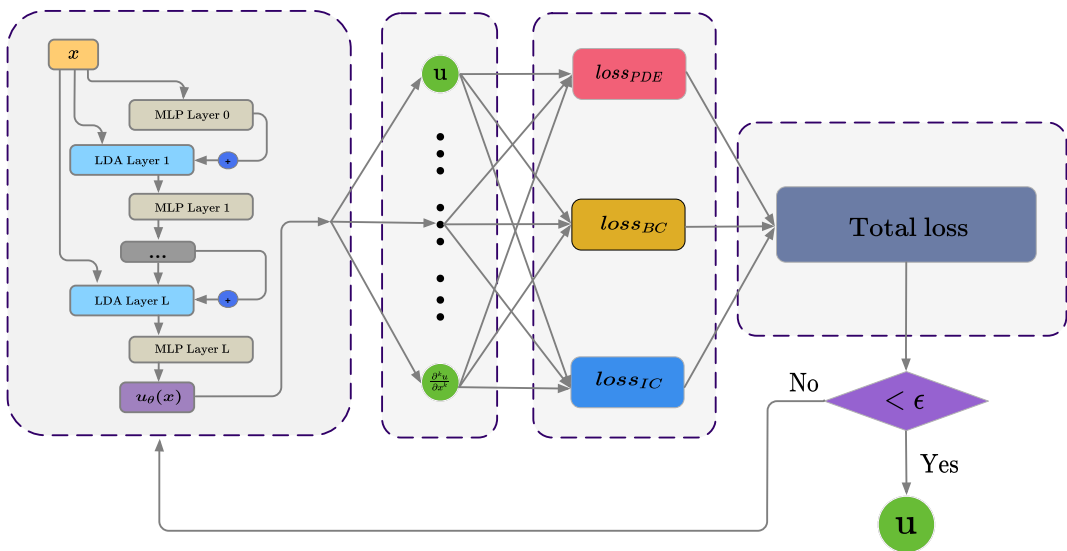


Figure 3: Overall architecture of the proposed LDA-PINN.

2.3 Conflict-Resolved Optimization

While the attentive architectural design introduced in the previous section improves the representational flexibility of PINNs, architectural enhancements alone do not fully address the training challenges encountered in practice. PINNs inherently involve multiple heterogeneous physical constraints, resulting in a multi-objective optimization problem where conflicting optimization signals may emerge during training. Therefore, beyond architectural design, it is essential to explicitly address optimization challenges in PINNs. In this subsection, we focus on conflict-resolved optimization strategies designed to mitigate destructive gradient interactions that arise from the multi-task nature of PINN training.

2.3.1 Gradient Conflicts from a Multi-Task PINN Perspective

Physics-Informed Neural Networks inherently lead to a multi-task learning (MTL) optimization problem, as multiple physical constraints are simultaneously enforced through a shared set of network parameters. In a standard PINN formulation, the total loss typically comprises several components, including the governing PDE residual loss, the initial condition (IC) loss, and the boundary condition (BC) loss. Each loss term corresponds to a distinct learning objective; however, all objectives are optimized with respect to the same parameter vector θ .

From an optimization perspective, this shared-parameter setting implies that each physical constraint contributes its own gradient.

$$\mathbf{g}_i = \nabla_{\theta} \mathcal{L}_i(\theta), \quad (16)$$

where \mathcal{L}_i denotes the loss of the i -th task. Ideally, these gradients would be mutually aligned, enabling cooperative updates that reduce all loss components simultaneously.

In practice, however, such alignment is seldom guaranteed during PINN training. The fundamental challenge arises from the inherent heterogeneity of physical constraints. The PDE residual enforces global dynamical consistency, whereas IC and BC losses impose localized constraints in space or time. These objectives differ significantly in physical meaning, numerical scale, and convergence behavior across training stages; consequently, they tend to produce gradients that point toward competing descent directions in parameter space. As a result, naively aggregating task gradients can lead to inconsistent optimization signals.

We formally characterize a *gradient conflict* between two tasks i and j when the inner product of their gradients is negative,

$$\mathbf{g}_i^\top \mathbf{g}_j < 0, \quad (17)$$

This indicates that an update direction that decreases the loss of one task may increase the loss of another. Geometrically, this condition corresponds to an obtuse angle between the gradient vectors, indicating destructive interference when the gradients are combined through simple summation. Figure 4 illustrates the geometric interpretation of cooperative and conflicting gradients.

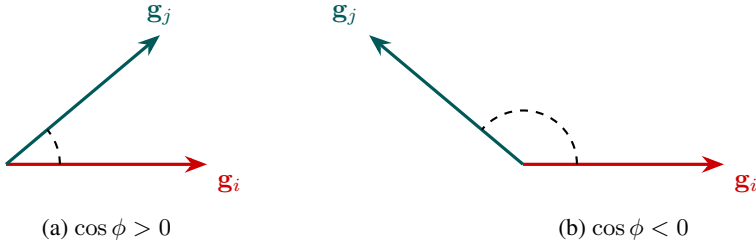


Figure 4: Geometric illustration of cooperative and conflicting gradients in multi-task PINN optimization.

In practice, such gradient conflicts are not isolated pathological events, but arise systematically in many PINN applications. The combination of heterogeneous physical objectives, non-convex loss landscapes, and multi-scale or high-frequency solution structures makes conflicting gradients a common occurrence throughout training. Consequently, standard gradient-based optimization with scalar loss aggregation may suffer from slow convergence, instability, or biased satisfaction of physical constraints.

Together, these observations suggest that gradient conflicts are intrinsic to PINN optimization in many practical settings and cannot be fully resolved by architectural expressiveness or loss reweighting alone. This perspective naturally calls for rethinking the above challenges through the lens of gradient-conflict-aware optimization, i.e., designing update rules that explicitly identify and mitigate conflicting task gradients in the shared parameter space.

2.3.2 Conflict-Resolved Gradient Strategies

The analysis above demonstrates that gradient conflicts naturally arise from the multi-task structure inherent in PINN training. This observation motivates the development of optimization strategies that explicitly and robustly mitigate such conflicts in a principled manner. A common approach in PINN optimization seeks to alleviate training imbalances through adaptive loss reweighting. Although reweighting strategies can partially compensate for disparities in gradient magnitudes, they fundamentally operate at the scalar level by rescaling loss terms. However, gradient conflicts arise from misalignment in the directional space of gradients rather than from magnitude imbalance alone. Consequently, even carefully tuned weights cannot prevent destructive interference when task gradients point in opposing descent directions. This limitation motivates the development of optimization strategies that explicitly operate within gradient space.

Inspired by recent advances in multi-task learning [22], we adopt a conflict-resolved gradient strategy based on *projecting conflicting gradients*, commonly known as PCGrad. The underlying design philosophy of this approach aligns closely with the requirements of PINN optimization. Specifically, it neither modifies the original loss formulation nor introduces auxiliary regularization terms, and it does not rely on task-specific or PDE-dependent heuristics. Moreover, it does not introduce any additional hyperparameters beyond those required by standard gradient-based optimizers. Instead, the method intervenes only when destructive gradient interactions are detected, making it a minimal yet principled modification to conventional optimization.

Formally, let $\mathbf{g}_i = \nabla_{\theta} \mathcal{L}_i(\theta)$ and $\mathbf{g}_j = \nabla_{\theta} \mathcal{L}_j(\theta)$ denote the gradients associated with two distinct PINN loss components. When their inner product satisfies

$$\mathbf{g}_i^T \mathbf{g}_j < 0, \quad (18)$$

a gradient conflict is identified [22]. In this case, the conflicting component of \mathbf{g}_i along the direction of \mathbf{g}_j is removed through orthogonal projection,

$$\mathbf{g}_i \leftarrow \mathbf{g}_i - \frac{\mathbf{g}_i^T \mathbf{g}_j}{\|\mathbf{g}_j\|^2} \mathbf{g}_j. \quad (19)$$

This operation preserves the non-conflicting component of \mathbf{g}_i while eliminating directions that would otherwise increase \mathcal{L}_j . The geometric interpretation of this projection is illustrated in Fig. 5, which depicts how destructive gradient components are removed under conflict.

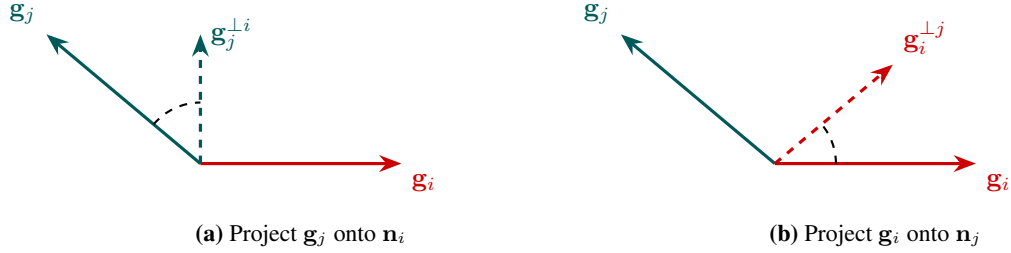


Figure 5: Geometric illustration of the two PCGrad projection directions under gradient conflict.

The projection procedure is applied across task gradients in a randomized order, and the final update direction is obtained by aggregating the adjusted gradients. An important property of this strategy is that it remains inactive when task gradients are cooperative. If $\mathbf{g}_i^T \mathbf{g}_j \geq 0$, no modification is applied, and the update reduces exactly to standard gradient aggregation. As a result, conflict-resolved optimization suppresses destructive interactions while preserving constructive multi-task learning. This selective intervention is especially advantageous in PINNs, where various physical constraints may predominate at different training stages or across spatial-temporal regions.

The complete procedure of the conflict-resolved optimization strategy is summarized in Algorithm 1. The algorithm operates directly in gradient space and is applied prior to gradient aggregation. By explicitly addressing gradient misalignment rather than scalar loss imbalance, conflict-resolved optimization overcomes a fundamental limitation of traditional loss reweighting schemes. In the following, this mechanism is incorporated into the PINN training pipeline, leading to a gradient-conflict-aware framework that improves optimization stability and physical consistency without altering the underlying loss structure.

Algorithm 1 Conflict-Resolved Gradient Optimization for PINNs

Require: Task losses $\{\mathcal{L}_k(\theta)\}_{k=1}^K$, shared parameters θ
Ensure: Conflict-resolved gradient \mathbf{g}^{CR}

- 1: Compute task gradients $\mathbf{g}_k \leftarrow \nabla_{\theta} \mathcal{L}_k(\theta)$, $k = 1, \dots, K$
- 2: Initialize projected gradients $\tilde{\mathbf{g}}_k \leftarrow \mathbf{g}_k$
- 3: **for** $i = 1$ to K **do**
- 4: Randomly permute task indices $\pi \subset \{1, \dots, K\} \setminus \{i\}$
- 5: **for** each $j \in \pi$ **do**
- 6: **if** $\tilde{\mathbf{g}}_i^{\top} \mathbf{g}_j < 0$ **then**
- 7: $\tilde{\mathbf{g}}_i \leftarrow \tilde{\mathbf{g}}_i - \frac{\tilde{\mathbf{g}}_i^{\top} \mathbf{g}_j}{\|\mathbf{g}_j\|_2^2} \mathbf{g}_j$
- 8: **end if**
- 9: **end for**
- 10: **end for**
- 11: Aggregate gradients $\mathbf{g}^{\text{CR}} \leftarrow \sum_{k=1}^K \tilde{\mathbf{g}}_k$
- 12: **return** \mathbf{g}^{CR}

2.3.3 Integration into PINNs and Discussion

The conflict-resolved gradient strategy described above can be integrated into the standard PINN training procedure, resulting in a gradient-conflict-aware framework referred to as *GC-PINN*. Notably, this integration functions solely at the optimization level and does not require any modifications to the physical loss formulation or the network architecture.

In a conventional PINN, multiple physical constraints—such as the PDE residual, initial condition, and boundary condition losses—are combined into a single objective function. Parameter updates are then computed by differentiating the weighted sum of these losses with respect to the shared parameters. By contrast, GC-PINN treats each loss component as a separate optimization task. After forward propagation and loss evaluation, task-specific gradients are computed independently and analyzed for pairwise conflicts within a dedicated resolution module.

As illustrated in Fig. 6, the primary distinction between GC-PINN and the standard PINN lies in the gradient aggregation stage. Rather than directly summing task gradients, GC-PINN incorporates a conflict resolution step before aggregation. When conflicting directions are detected, destructive components are removed through orthogonal projection, and the adjusted gradients are then aggregated to form the final update. If no conflicts are present, the update reduces precisely to that of a standard PINN, ensuring backward compatibility.

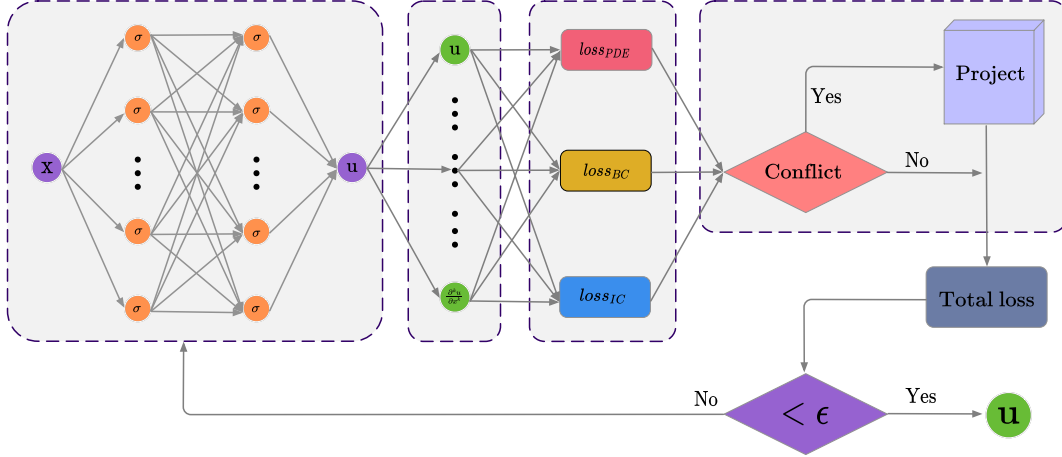


Figure 6: Overall framework of the proposed GC-PINN.

This design preserves the physical interpretation of each loss term, introduces no additional hyperparameters, and remains fully compatible with commonly used optimizers such as Adam and SGD, intervening selectively only when gradient conflicts arise. From a broader perspective, GC-PINN complements architectural improvements. While enhanced network architectures—such as the proposed LDA mechanism—increase the representational capacity of PINNs, GC-PINN tackles a different bottleneck by reducing destructive interactions among heterogeneous physical

constraints within the shared parameter space. Together, these approaches promote stable and balanced training without modifying the core PINN formulation.

2.4 Architecture–Optimization Co-Design

Despite recent advances in architectural design and optimization techniques for PINNs, many challenging PDE problems remain difficult to solve in a stable and reliable manner. A fundamental reason is that architectural representation and optimization dynamics are often treated as separate design choices, despite being intrinsically linked through gradient flow during training. In PINNs, the learned representation defines the geometry and distribution of task gradients within the shared parameter space, while gradient-based optimization controls the interaction of competing physical objectives through these gradients.

The LDA mechanism introduced in Section 2.2 not only enhances representational flexibility but also reshapes the propagation of information and gradients across network layers. By reintroducing and adaptively modulating the input coordinates at each hidden layer, LDA promotes a more distributed and input-conditioned representation. Compared to standard MLP-based PINNs—where gradients related to different physical constraints often concentrate on a limited subset of parameters—LDA redistributes gradient contributions across layers and parameter subspaces. This redistribution improves the conditioning of the optimization landscape and produces more structured gradient patterns.

Conflict-resolved optimization strategies operate explicitly in gradient space, however, their effectiveness depends critically on the geometric structure of task gradients. When gradients induced by different physical constraints are highly entangled, projection-based conflict mitigation can become unstable or overly aggressive. The representational flexibility introduced by LDA promotes task separability in gradient space, yielding gradients that more distinctly reflect individual physical objectives. As a result, conflict detection becomes more informative, enabling conflict mitigation to be applied in a more targeted and stable manner.

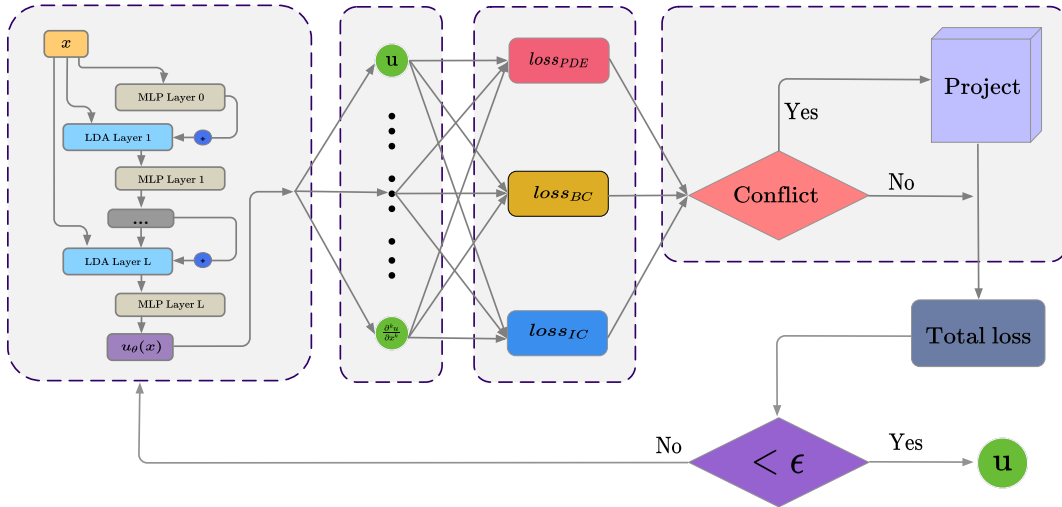


Figure 7: Overall framework of the proposed ACR-PINN.

From this perspective, LDA and conflict-resolved optimization address complementary aspects of PINN training. The attentive architecture governs how physical information is encoded and distributed within the network, while conflict-resolved optimization manages the interaction of heterogeneous physical objectives during parameter updates. Their combined effect cannot be reduced to a simple superposition of architectural and optimization improvements. Instead, the architecture reshapes the gradient landscape, enabling the optimizer to more effectively reconcile competing constraints, thereby improving stability and convergence.

By integrating LDA with conflict-resolved gradient optimization, we develop a unified framework termed the *Architecture–Conflict-Resolved PINN (ACR-PINN)*. As illustrated in Fig. 7, ACR-PINN replaces the standard MLP backbone with an LDA-enhanced network and augments the training pipeline with a gradient conflict resolution module, while keeping the physical loss formulation unchanged. This architecture–optimization co-design produces a robust and scalable PINN framework for solving complex, multi-constraint partial differential equations.

Algorithm 2 summarizes the complete training procedure of ACR-PINN, explicitly integrating the proposed architecture–optimization co-design into a unified optimization loop. In each training iteration, the LDA-enhanced network

Algorithm 2 Training Procedure of ACR-PINN

Require: Training sets $\mathcal{D}_f, \mathcal{D}_{ic}, \mathcal{D}_{bc}$; parameters θ of LDA-network u_θ ; optimizer $\text{Opt}(\cdot)$ with step size η ; epochs N
Ensure: Trained parameters θ

- 1: **for** $n = 1$ to N **do**
- 2: Sample collocation points $(x_f, t_f) \sim \mathcal{D}_f$
- 3: Sample IC points $(x_i, t_0) \sim \mathcal{D}_{ic}$ and BC points $(x_b, t_b) \sim \mathcal{D}_{bc}$
- 4: Evaluate the LDA-enhanced PINN on different constraint sets:
- 5: $\hat{u}_f \leftarrow u_\theta(x_f, t_f), \hat{u}_{ic} \leftarrow u_\theta(x_i, t_0), \hat{u}_{bc} \leftarrow u_\theta(x_b, t_b)$
- 6: Compute task losses:
- 7: $\mathcal{L}_{\text{PDE}} \leftarrow \frac{1}{N_f} \sum \|\mathcal{N}[\hat{u}_f]\|_2^2$
- 8: $\mathcal{L}_{\text{IC}} \leftarrow \frac{1}{N_i} \sum \|\hat{u}_{ic} - u_0\|_2^2$
- 9: $\mathcal{L}_{\text{BC}} \leftarrow \frac{1}{N_b} \sum \|\hat{u}_{bc} - u_b\|_2^2$
- 10: Compute per-task gradients:
- 11: $\mathbf{g}_1 \leftarrow \nabla_\theta \mathcal{L}_{\text{PDE}}, \mathbf{g}_2 \leftarrow \nabla_\theta \mathcal{L}_{\text{IC}}, \mathbf{g}_3 \leftarrow \nabla_\theta \mathcal{L}_{\text{BC}}$
- 12: Initialize projected gradients: $\tilde{\mathbf{g}}_k \leftarrow \mathbf{g}_k$ for $k \in \{1, 2, 3\}$
- 13: **for** $i \in \{1, 2, 3\}$ **do**
- 14: Draw a random order π of $\{1, 2, 3\} \setminus \{i\}$
- 15: **for each** $j \in \pi$ **do**
- 16: **if** $\langle \tilde{\mathbf{g}}_i, \mathbf{g}_j \rangle < 0$ **then**
- 17: $\tilde{\mathbf{g}}_i \leftarrow \tilde{\mathbf{g}}_i - \frac{\langle \tilde{\mathbf{g}}_i, \mathbf{g}_j \rangle}{\|\mathbf{g}_j\|_2^2} \mathbf{g}_j$
- 18: **end if**
- 19: **end for**
- 20: **end for**
- 21: Aggregate conflict-resolved gradient:
- 22: $\mathbf{g}^{\text{CR}} \leftarrow \tilde{\mathbf{g}}_1 + \tilde{\mathbf{g}}_2 + \tilde{\mathbf{g}}_3$
- 23: Update parameters:
- 24: $\theta \leftarrow \text{Opt}(\theta; \mathbf{g}^{\text{CR}}, \eta)$
- 25: **end for**

first generates input-conditioned representations corresponding to various physical constraints. Task-specific losses corresponding to the PDE residual, initial condition, and boundary condition are then evaluated, and their gradients are computed independently. Prior to parameter updates, a PCGrad-style projection is applied in the gradient space to resolve destructive conflicts among \mathcal{L}_{PDE} , \mathcal{L}_{IC} , and \mathcal{L}_{BC} . The resulting conflict-resolved gradient is then used to update the network parameters through a standard gradient-based optimizer.

3 Experiments

In this section, we present a comprehensive experimental evaluation of the proposed framework using a set of representative PDEs, including the Burgers equation, the Helmholtz equation, the Klein–Gordon equation, and the lid-driven cavity flow problem. These benchmarks encompass nonlinear dynamics, multiscale behaviors, and strongly constrained physical systems, thereby providing a rigorous testbed for evaluating both the representational capacity and optimization robustness of Physics-Informed Neural Networks.

For each PDE problem, the collocation points used to evaluate the PDE residual, along with the points enforcing the initial and boundary conditions, are sampled once and shared across all compared models. Interior collocation points are generated using Latin Hypercube Sampling (LHS) to ensure uniform coverage of the spatiotemporal domain, while initial and boundary condition points are sampled according to their respective constraint definitions. All sampling procedures are fully determined by fixed random seeds, eliminating variability introduced during data generation and ensuring fair model comparisons.

To minimize the effects of random initialization and stochastic optimization, each experiment is repeated five times using different random seeds: $\{1234, 1235, 1236, 1237, 1238\}$. All quantitative results reported in the following sections are derived by aggregating statistics from these independent runs.

Model accuracy is assessed using both the relative L_2 error and the relative L_∞ error, which are defined, respectively, as

$$\varepsilon_{L_2} = \frac{\|u_{\text{pred}} - u_{\text{exact}}\|_{L_2(\Omega)}}{\|u_{\text{exact}}\|_{L_2(\Omega)}}, \quad \varepsilon_{L_\infty} = \frac{\|u_{\text{pred}} - u_{\text{exact}}\|_{L_\infty(\Omega)}}{\|u_{\text{exact}}\|_{L_\infty(\Omega)}}, \quad (20)$$

where u_{pred} and u_{exact} denote the predicted and exact solutions, respectively, and Ω represents the computational domain.

The relative L_2 error measures the global approximation accuracy in an energy-averaged sense, whereas the relative L_∞ error quantifies the maximum pointwise deviation and is especially sensitive to localized errors or sharp features in the solution. Reporting both metrics enables a more comprehensive evaluation of model performance across the entire domain, as well as in worst-case scenarios.

All models are trained using the Adam optimizer with the same hyperparameter settings. No method-specific or PDE-specific hyperparameter tuning was performed, ensuring that the observed performance differences primarily reflect the impact of architectural design and optimization strategy rather than task-dependent parameter adjustments.

3.1 Burgers equation

We first consider the one-dimensional Burgers equation as a benchmark problem[32]. This equation represents a classical nonlinear PDE that captures key features of viscous transport and nonlinear advection. It is commonly used to evaluate both approximation accuracy and training stability in physics-informed learning frameworks.

The governing equation reads

$$u_t + u u_x = \nu u_{xx}, \quad (21)$$

posed on the space–time domain

$$(x, t) \in \Omega = [-1, 1] \times [0, 1]. \quad (22)$$

The system is equipped with the initial condition

$$u(x, 0) = -\sin(\pi x), \quad (23)$$

together with homogeneous Dirichlet boundary conditions

$$u(-1, t) = u(1, t) = 0, \quad t \in [0, 1]. \quad (24)$$

The viscosity coefficient is fixed as

$$\nu = \frac{0.01}{\pi}. \quad (25)$$

For training, the dataset comprises 100 points sampled from the initial condition, 100 points from the boundary conditions, and 10,000 interior collocation points generated via Latin Hypercube Sampling over Ω .

Unless otherwise stated, all compared models share the same network configuration: two input neurons corresponding to the spatial coordinate x and time t , four hidden layers with 20 neurons each, using \tanh activation functions; and a single output neuron representing the solution $u(x, t)$.

Table 1: Comparison of relative L_2 and L_∞ errors for the Burgers' equation.

Model	Iterations	$\bar{\varepsilon}_{L_2} \pm \sigma(\varepsilon_{L_2})$	$\bar{\varepsilon}_{L_\infty} \pm \sigma(\varepsilon_{L_\infty})$
Std-PINN	40000	$9.96 \times 10^{-3} \pm 5.59 \times 10^{-3}$	$1.03 \times 10^{-1} \pm 6.26 \times 10^{-2}$
LDA-PINN	40000	$2.60 \times 10^{-3} \pm 1.89 \times 10^{-3}$	$2.15 \times 10^{-2} \pm 1.93 \times 10^{-2}$
GC-PINN	40000	$4.68 \times 10^{-3} \pm 2.38 \times 10^{-3}$	$3.38 \times 10^{-2} \pm 1.33 \times 10^{-2}$
ACR-PINN	40000	$9.15 \times 10^{-4} \pm 1.15 \times 10^{-4}$	$6.74 \times 10^{-3} \pm 1.57 \times 10^{-3}$

Table 1 presents a quantitative comparison of the relative L_2 and L_∞ errors for the Burgers equation across all four models, with statistics aggregated over five independent runs. The standard PINN exhibits relatively large errors, especially in the L_∞ norm, indicating challenges in accurately capturing localized sharp gradients associated with shock formation. In addition, the relatively large standard deviation indicates sensitivity to random initialization and optimization dynamics. Incorporating the proposed layer-wise dynamic attention architecture results in a significant improvement in accuracy. As demonstrated by the results of LDA-PINN, the relative L_2 error is reduced by nearly an order of magnitude compared to the standard PINN, accompanied by a substantial decrease in the L_∞ error.

This improvement suggests that dynamically re-encoding and modulating input coordinates at each hidden layer enhances the network’s ability to capture the multi-scale solution structures inherent in the Burgers equation. The GC-PINN, which incorporates conflict-resolved gradient optimization while maintaining a standard MLP backbone, also demonstrates consistent performance improvements over the baseline. Both error metrics have decreased, and the variability across independent runs is significantly lower than that observed with the standard PINN. These results indicate that explicitly mitigating gradient conflicts among the PDE residual, initial condition, and boundary condition losses contributes to more stable and balanced training, even in the absence of architectural modifications. Among all the methods, the proposed ACR-PINN achieves the best overall performance. As shown in Table 1, ACR-PINN achieves the lowest relative L_2 and L_∞ errors with the smallest standard deviation, demonstrating superior accuracy and robustness. Compared to the standard PINN, the relative L_2 error is reduced by more than an order of magnitude. This result highlights the synergistic effect of combining attentive representation learning with conflict-resolved gradient optimization, thereby validating the effectiveness of the proposed architecture-optimization co-design.

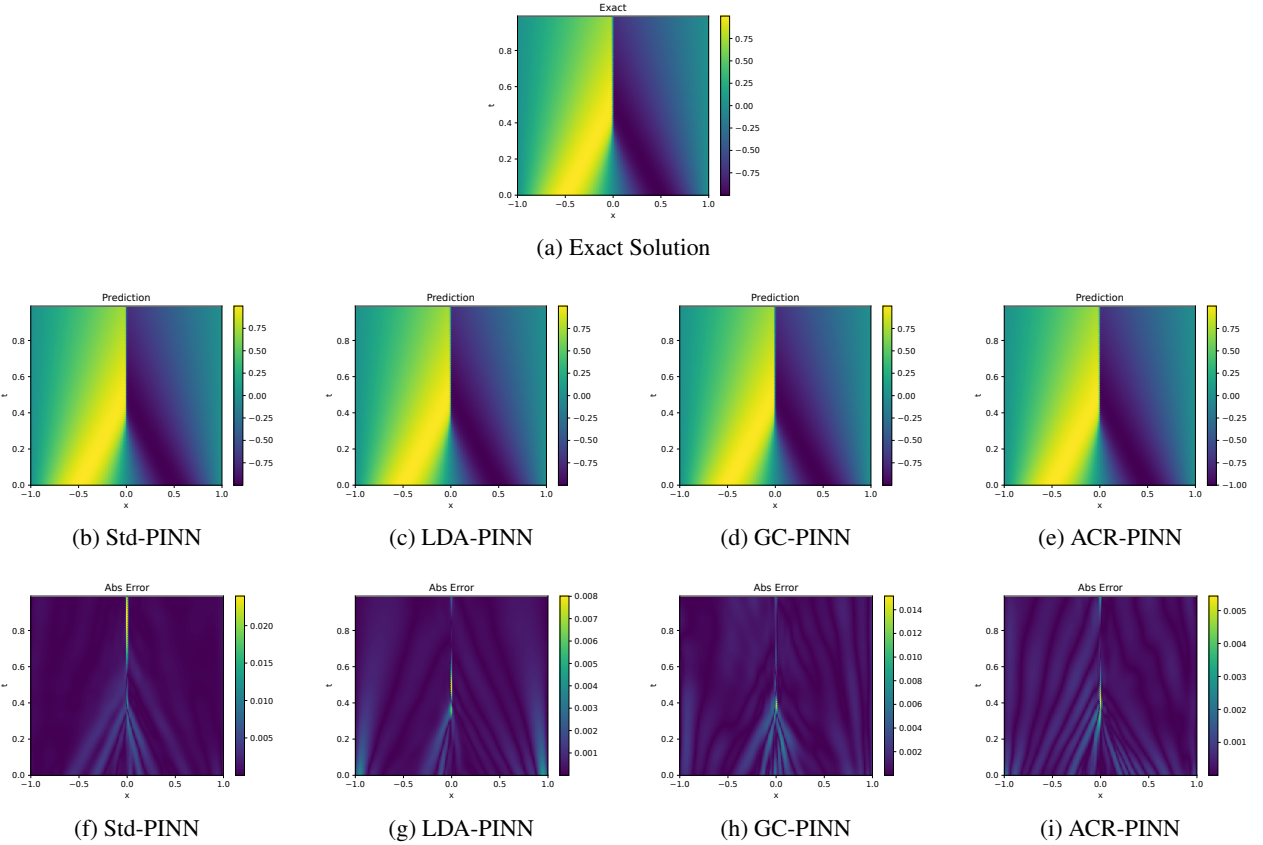


Figure 8: Visualization of the exact solution, predicted solutions, and absolute error distributions for the Burgers’ equation.

Figure 8 compares the exact solution, predicted solutions, and absolute error distributions generated by different models for the Burgers equation. The standard PINN captures the overall solution trend but exhibits pronounced error concentrations near regions with steep gradients, particularly around the shock-like structure. These localized errors indicate a limited resolution capability under strong nonlinearity. Incorporating the layer-wise dynamic attention mechanism substantially improves prediction quality. LDA-PINN produces smoother solution fields with noticeably reduced error magnitudes across the domain, especially in the interior region. This improvement reflects the benefit of reintroducing and adaptively modulating input coordinates at each hidden layer, enhancing the network’s ability to represent multi-scale solution features. GC-PINN further suppresses error accumulation by mitigating destructive interactions among competing physical constraints during training. Although its backbone architecture remains unchanged, the conflict-resolved optimization leads to more balanced error distributions compared to the standard PINN. Among all models, ACR-PINN achieves the most accurate reconstruction, exhibiting uniformly low error levels throughout the space-time domain.

To further evaluate solution fidelity near the final time, Fig. 9 presents the predicted solutions and corresponding absolute errors at $t = 0.99$. The standard PINN exhibits pronounced deviations near the shock region, where sharp gradients dominate the solution behavior. LDA-PINN significantly sharpens the solution profile and reduces peak errors, demonstrating improved resolution of localized structures. GC-PINN diminishes oscillatory errors and produces more consistent predictions across the spatial domain, confirming the stabilizing effect of conflict-resolved gradient updates. In contrast, ACR-PINN most closely matches the reference solution, achieving the smallest pointwise errors throughout the entire interval. This result highlights the combined advantage of enhanced representation and gradient-level conflict mitigation in resolving sharp solution features.

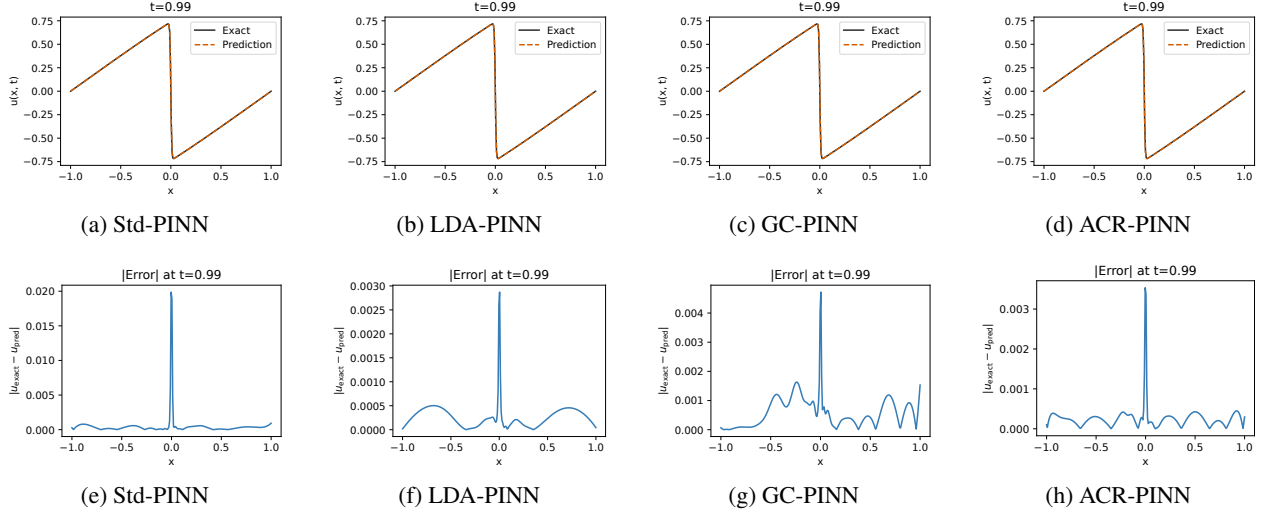


Figure 9: Time-slice comparison of predicted solutions and absolute errors for the Burgers' equation at $t = 0.99$.

The training dynamics are illustrated in Fig. 10, which compares the evolution of relative L_2 and L_∞ errors across all models. The standard PINN converges slowly and exhibits noticeable fluctuations, indicating instability caused by competing gradient directions arising from heterogeneous physical constraints. LDA-PINN converges more rapidly and attains a lower error level, benefiting from enhanced representational flexibility and more distributed gradient propagation. GC-PINN demonstrates smoother and more stable convergence curves, confirming that conflict-resolved gradient updates effectively suppress destructive interference during training. Notably, ACR-PINN achieves both the fastest convergence and the lowest final errors, suggesting that its attentive architecture reshapes the gradient landscape in a manner that can be effectively exploited by conflict-resolved optimization.

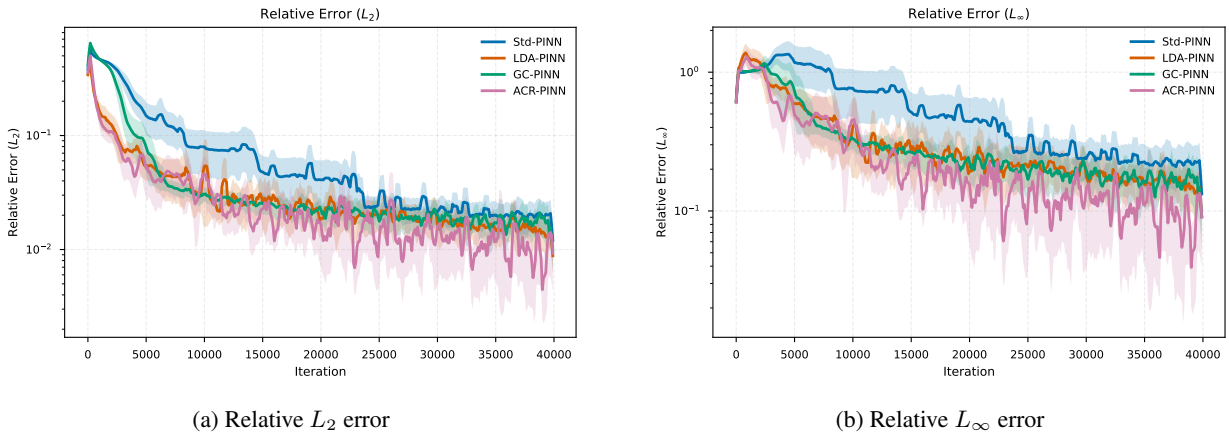


Figure 10: Comparison of relative L_2 and L_∞ errors for all models during training.

Overall, the Burgers' equation experiments demonstrate the complementary roles of architectural enhancements and optimization strategies. The LDA mechanism primarily enhances representational capacity by enabling layer-wise

reinterpretation of input coordinates, thereby alleviating gradient concentration. Conflict-resolved optimization directly addresses destructive interactions among heterogeneous physical constraints at the gradient level. Their integration within ACR-PINN produces a synergistic improvement in accuracy, stability, and robustness, validating the effectiveness of the proposed architecture–optimization co-design for challenging nonlinear PDE problems.

3.2 Helmholtz equation

The Helmholtz equation is a fundamental partial differential equation that arises in steady-state wave phenomena, with applications in acoustics, electromagnetism, and quantum mechanics [33]. Due to its oscillatory solutions and sensitivity to frequency, it is widely used to evaluate the capability of numerical methods in capturing high-frequency and multi-scale behaviors.

In this study, we consider the two-dimensional Helmholtz equation

$$\frac{\partial^2 u}{\partial x^2} + \frac{\partial^2 u}{\partial y^2} + k^2 u = q(x, y), \quad (26)$$

where $u(x, y)$ denotes the wave field, k is the wave number, and $q(x, y)$ is a prescribed source term.

Following the benchmark setting in [14], the source term is chosen as

$$q(x, y) = [-(a_1\pi)^2 - (a_2\pi)^2 + k^2] \sin(a_1\pi x) \sin(a_2\pi y), \quad (27)$$

which admits the analytical solution

$$u(x, y) = \sin(a_1\pi x) \sin(a_2\pi y). \quad (28)$$

The computational domain is defined as $(x, y) \in [-1, 1] \times [-1, 1]$ and is subject to homogeneous Dirichlet boundary conditions,

$$u(-1, y) = u(1, y) = u(x, -1) = u(x, 1) = 0, \quad (29)$$

corresponding to a perfectly reflecting square cavity.

To examine the influence of solution frequency on PINN performance, we consider two representative configurations by varying the mode numbers (a_1, a_2) while keeping all other parameters fixed. Specifically, the wave number is set to $k = 1$, and the two test cases are given by

$$(a_1, a_2) = (1, 4) \quad \text{and} \quad (a_1, a_2) = (4, 4), \quad (30)$$

which correspond to moderate-frequency and high-frequency regimes, respectively.

For both cases, boundary points are sampled uniformly along the domain boundary, while interior collocation points are generated using Latin Hypercube Sampling (LHS). Unless otherwise specified, all models use the same neural network configuration: an input layer with two neurons corresponding to the spatial coordinates (x, y) , followed by four hidden layers with 50 neurons each, employing \tanh activation functions, and a single output neuron representing $u(x, y)$. All network parameters are initialized using the Xavier initialization scheme.

This unified experimental setup enables a controlled comparison across different frequency regimes, ensuring that observed performance differences primarily reflect the effects of architectural design and optimization strategies rather than variations in problem configurations.

3.2.1 High-Frequency Case: $(a_1, a_2) = (1, 4)$

Table 2 summarizes the quantitative performance of the four PINN-based models on the moderate-frequency Helmholtz problem with parameters $(a_1, a_2) = (1, 4)$. Both the relative L_2 and L_∞ errors are reported as the mean and standard deviation calculated over five independent runs.

Table 2: Comparison of relative L_2 and L_∞ errors for the Helmholtz equation with $a_1 = 1$ and $a_2 = 4$.

Model	Iterations	$\bar{\varepsilon}_{L_2} \pm \sigma(\varepsilon_{L_2})$	$\bar{\varepsilon}_{L_\infty} \pm \sigma(\varepsilon_{L_\infty})$
Std-PINN	40000	$1.77 \times 10^{-1} \pm 5.48 \times 10^{-2}$	$5.15 \times 10^{-1} \pm 1.02 \times 10^{-1}$
LDA-PINN	40000	$3.06 \times 10^{-2} \pm 7.21 \times 10^{-3}$	$1.66 \times 10^{-1} \pm 2.02 \times 10^{-2}$
GC-PINN	40000	$8.63 \times 10^{-3} \pm 8.05 \times 10^{-4}$	$6.84 \times 10^{-2} \pm 1.41 \times 10^{-2}$
ACR-PINN	40000	$8.16 \times 10^{-3} \pm 1.96 \times 10^{-3}$	$5.16 \times 10^{-2} \pm 1.82 \times 10^{-2}$

The standard PINN demonstrates limited accuracy, with a mean relative L_2 error on the order of 10^{-1} and a pronounced L_∞ error exceeding 0.5. These results indicate that even at moderate spatial frequencies, the vanilla MLP-based PINN struggles to accurately resolve oscillatory solution structures and maintain uniform pointwise accuracy across the domain. Introducing the LDA architecture leads to substantial improvement. Compared to the standard PINN, LDA-PINN reduces the mean L_2 error by nearly an order of magnitude, reflecting enhanced representational capability for spatially varying wave patterns. Nevertheless, the remaining variance across runs suggests that optimization-related difficulties persist when multiple physical constraints are enforced simultaneously. GC-PINN further improves numerical accuracy by explicitly mitigating gradient conflicts during training. Relative to LDA-PINN, GC-PINN achieves a lower L_2 error along with a noticeable reduction in the L_∞ error, indicating a more balanced satisfaction of the PDE residual and boundary constraints. This observation confirms that conflict-resolved optimization is effective even when the underlying network architecture remains unchanged. Among all methods, the proposed ACR-PINN consistently delivers the best overall performance, achieving the lowest mean errors in both norms and reduced variance across independent runs, thereby demonstrating improved robustness and training stability. These results highlight a clear synergistic benefit from the combined incorporation of attentive representation learning and conflict-resolved gradient optimization.

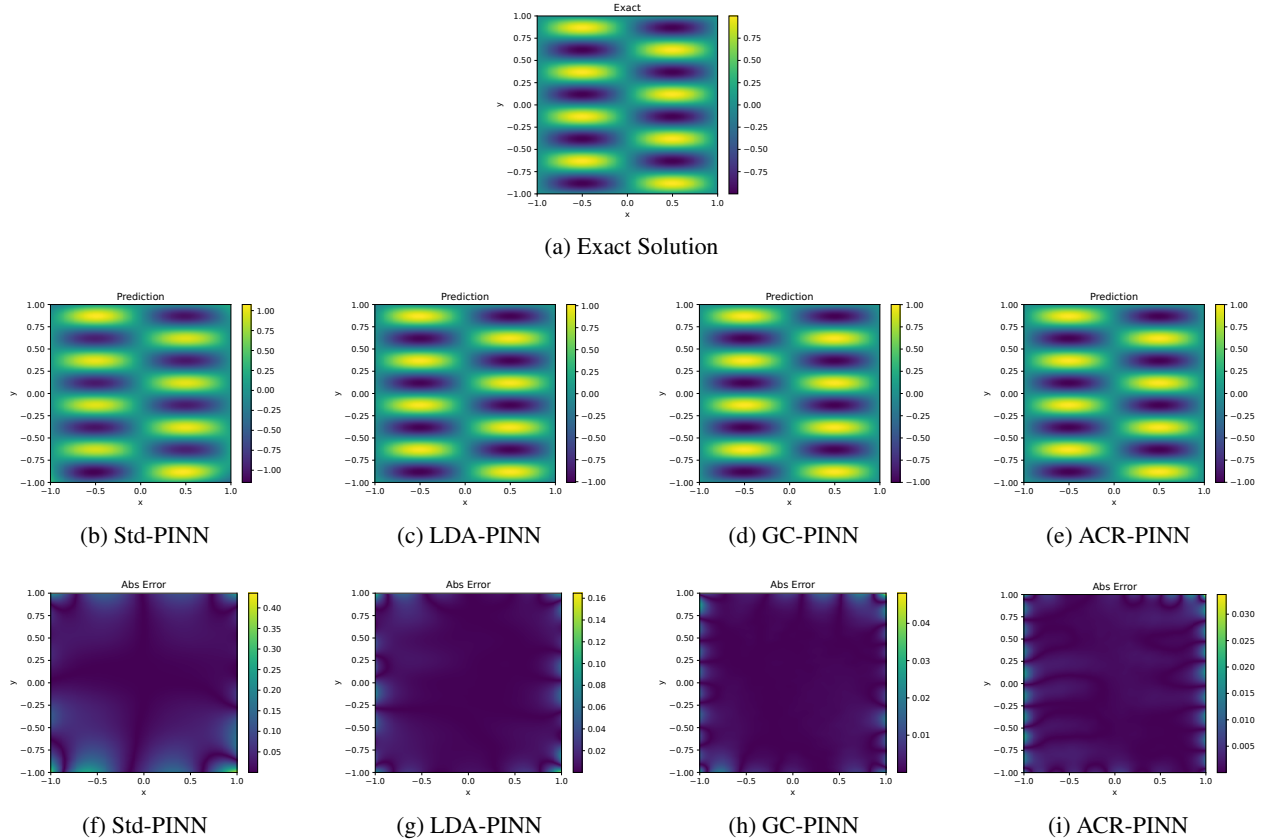


Figure 11: Visualization of the exact solution, predicted solutions, and absolute error distributions for the Helmholtz equation with $a_1 = 1$ and $a_2 = 4$.

Figure 11 compares the exact solution, predicted solutions, and absolute error distributions produced by different models for the Helmholtz equation with parameters $(a_1, a_2) = (1, 4)$. The standard PINN exhibits noticeable amplitude distortion and spatial phase mismatch, particularly in regions with pronounced oscillations, indicating a limited ability to resolve wave-like solution structures. Introducing the layer-wise dynamic attention mechanism results in a visibly smoother approximation and improved global structure; however, localized error regions persist, suggesting that architectural enhancements alone do not fully address the optimization imbalance caused by multiple physical constraints. GC-PINN further reduces large error concentrations, especially near boundary-adjacent regions where competing constraints are most pronounced. Among all models, ACR-PINN provides the closest match to the exact

solution, with uniformly reduced error magnitudes across the domain and no evident localized distortion, demonstrating the combined benefits of attentive representation learning and conflict-resolved optimization.

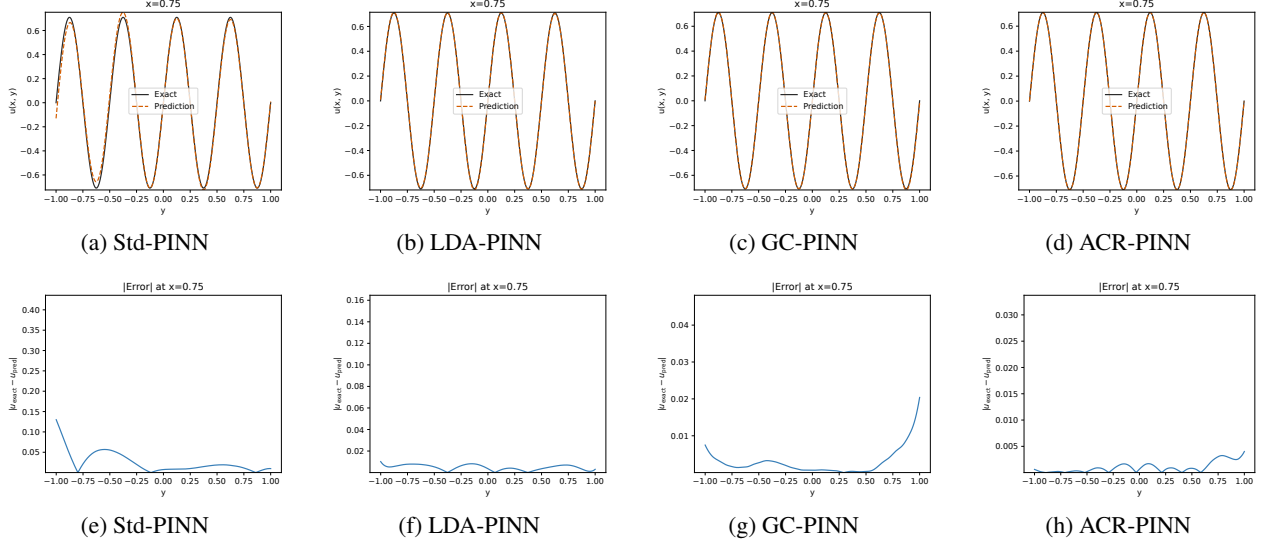


Figure 12: Spatial slice comparison of predicted solutions and absolute errors for the Helmholtz equation with $a_1 = 1$ and $a_2 = 4$ at $x = 0.75$.

To further evaluate local accuracy, Fig. 12 shows the predicted solutions and absolute error profiles along the spatial slice $x = 0.75$. The standard PINN exhibits noticeable phase shifts and amplitude deviations, while LDA-PINN captures the dominant oscillatory pattern but still shows residual discrepancies near the extrema. GC-PINN enhances pointwise accuracy across the slice, especially in regions with rapid variation. In contrast, ACR-PINN achieves the most accurate slice-wise reconstruction, with minimal phase error and significantly reduced pointwise absolute error, demonstrating its superior capability in resolving oscillatory Helmholtz solutions.

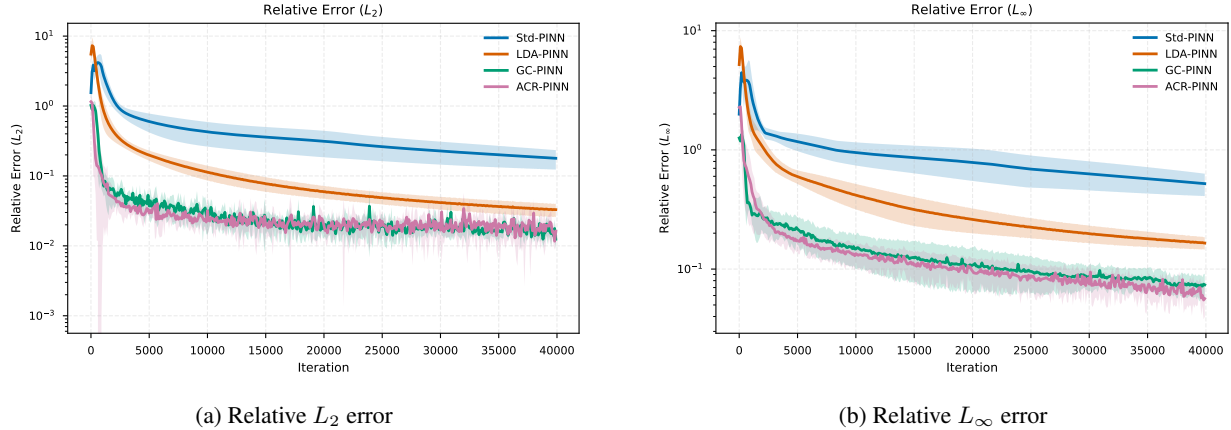


Figure 13: Comparison of relative L_2 and L_∞ errors for all models on the Helmholtz equation with $a_1 = 1$ and $a_2 = 4$.

The evolution of the relative L_2 and L_∞ errors during training, shown in Fig. 13, highlights clear differences in both convergence speed and stability among the models compared. The standard PINN converges slowly and saturates at a relatively high error level. LDA-PINN accelerates early-stage error reduction but tends to plateau prematurely, indicating that improved representation alone is insufficient to fully reconcile competing physical constraints.

The error trajectories of GC-PINN and ACR-PINN exhibit mild oscillations during training, which can be attributed to the conflict-resolved update mechanism: gradient projection is activated only when conflicts are detected and is applied in a randomized order, resulting in non-smooth but conflict-aware update directions. Despite these fluctuations, both methods achieve substantially lower error floors than Std-PINN and LDA-PINN, demonstrating enhanced robustness

under multi-constraint optimization. Notably, ACR-PINN consistently attains the lowest final errors in both norms, underscoring the effectiveness of jointly integrating attentive representations with conflict-resolved optimization.

This case demonstrates that for moderately oscillatory solutions, enhancing representational capacity already produces substantial accuracy improvements, while conflict-resolved optimization is essential for stabilizing training and refining convergence.

3.2.2 High-Frequency Case: $(a_1, a_2) = (4, 4)$

We next consider a more challenging high-frequency Helmholtz problem with mode numbers $(a_1, a_2) = (4, 4)$, where the solution exhibits dense oscillatory patterns along both spatial directions. Compared to the moderate-frequency setting, this case imposes significantly greater demands on both representation and optimization due to pronounced spectral bias, intensified multi-scale interactions, and more frequent gradient conflicts among physical constraints.

Table 3: Comparison of relative L_2 and L_∞ errors for the Helmholtz equation with $a_1 = 4$ and $a_2 = 4$.

Model	Iterations	$\bar{\varepsilon}_{L_2} \pm \sigma(\varepsilon_{L_2})$	$\bar{\varepsilon}_{L_\infty} \pm \sigma(\varepsilon_{L_\infty})$
Std-PINN	40000	$1.65 \times 10^{-1} \pm 2.18 \times 10^{-2}$	$6.89 \times 10^{-1} \pm 6.14 \times 10^{-2}$
LDA-PINN	40000	$9.24 \times 10^{-2} \pm 1.35 \times 10^{-2}$	$5.72 \times 10^{-1} \pm 1.62 \times 10^{-1}$
GC-PINN	40000	$2.11 \times 10^{-2} \pm 1.35 \times 10^{-3}$	$2.72 \times 10^{-1} \pm 8.08 \times 10^{-2}$
ACR-PINN	40000	$1.92 \times 10^{-2} \pm 3.74 \times 10^{-3}$	$1.85 \times 10^{-1} \pm 5.15 \times 10^{-2}$

The quantitative results summarized in Table 3 reveal a significant decline in the performance of the standard PINN as the solution frequency increases. Std-PINN fails to accurately resolve the oscillatory structure, yielding a relative L_2 error of 1.65×10^{-1} and an even larger L_∞ error exceeding 6.8×10^{-1} . Such large peak-wise errors indicate severe local inaccuracies and are characteristic manifestations of spectral bias in high-frequency regimes. Incorporating the layer-wise dynamic attention architecture partially alleviates these difficulties. LDA-PINN reduces the relative L_2 error by approximately 44% compared to Std-PINN, demonstrating that enhanced representational flexibility facilitates the approximation of oscillatory solution components. However, the persistently large L_∞ error and its relatively high variance suggest that architectural improvements alone are insufficient to fully stabilize training when strong multi-constraint interactions are present. GC-PINN exhibits markedly different behavior. By explicitly resolving gradient conflicts during optimization, GC-PINN achieves an order-of-magnitude reduction in the relative L_2 error compared to the standard PINN. This improvement highlights that optimization instability becomes a dominant bottleneck in the high-frequency setting. Nevertheless, the remaining L_∞ error remains comparatively large, indicating that while conflict-resolved optimization enhances global convergence, it cannot fully compensate for limited representational capacity. Among all models, the proposed ACR-PINN consistently delivers the best overall performance. It attains the lowest errors in both L_2 and L_∞ norms, along with reduced variance across independent runs, reflecting improved robustness and reliability. These results demonstrate that in high-frequency Helmholtz problems, neither architectural enhancement nor optimization refinement alone is sufficient. Instead, simultaneously improving representation quality and mitigating gradient conflicts is essential for achieving accurate and stable PINN solutions.

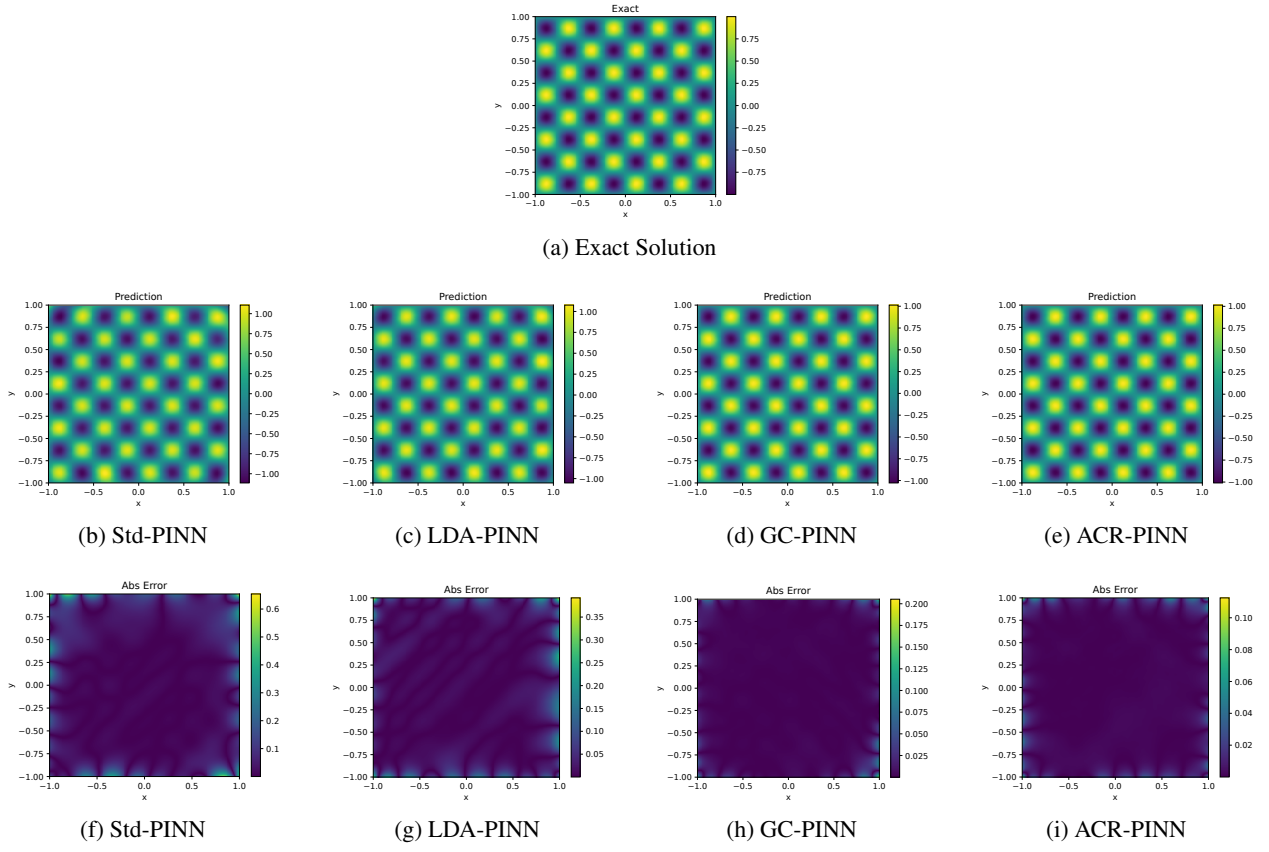


Figure 14: Visualization of the exact solution, predicted solutions, and absolute error distributions for the Helmholtz equation with $a_1 = 4$ and $a_2 = 4$.

Figure 14 compares the exact solution with the predicted solutions and absolute error distributions generated by different models for the high-frequency Helmholtz problem. The standard PINN exhibits severe spatial distortions, with large error regions distributed throughout the domain, particularly near oscillatory extrema, indicating a pronounced inability to resolve dense wave patterns. Introducing the layer-wise dynamic attention mechanism improves the global structure of the solution, as LDA-PINN captures the dominant oscillatory modes more clearly; however, noticeable localized errors persist in regions of rapid spatial variation. GC-PINN further suppresses large-scale error accumulation and produces smoother solution fields, yet residual discrepancies remain visible, reflecting limitations in representational capacity. In contrast, ACR-PINN achieves the closest agreement with the exact solution, with uniformly reduced error magnitudes and no prominent localized distortion regions, highlighting the complementary benefits of attentive representation learning and conflict-resolved optimization.

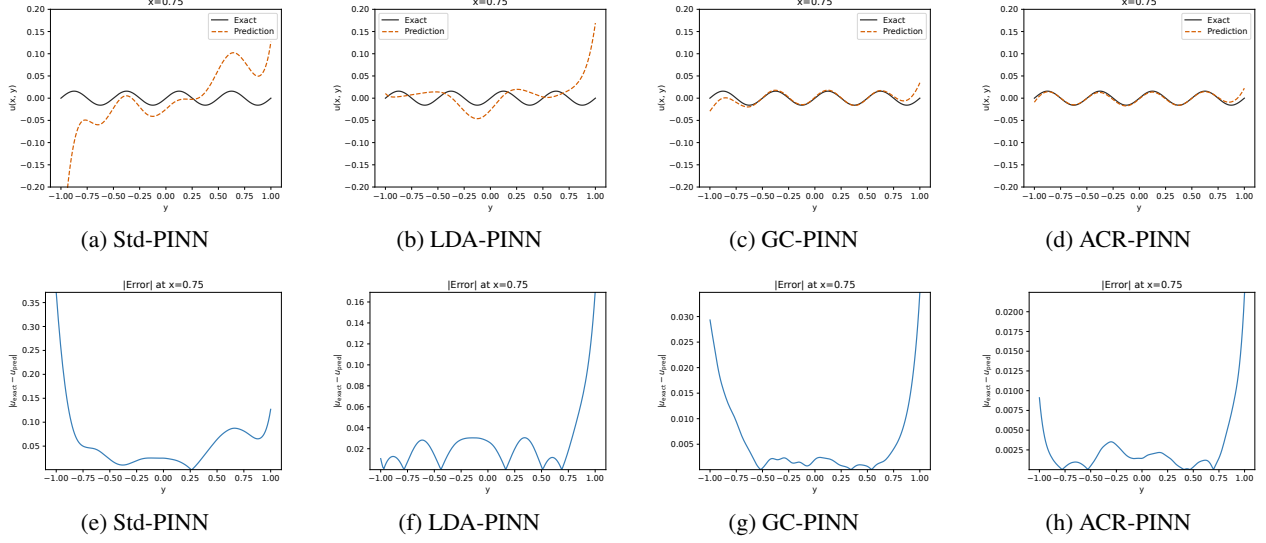


Figure 15: Spatial slice comparison of predicted solutions and absolute errors for the Helmholtz equation with $a_1 = 4$ and $a_2 = 4$ at $x = 0.75$.

The spatial slice comparison at $x = 0.75$, shown in Fig. 15, further highlights the differences among the models. The standard PINN fails to accurately track the oscillatory profile, exhibiting noticeable phase shifts and amplitude mismatches along the slice. LDA-PINN improves phase alignment but still underestimates peak amplitudes, resulting in visible deviations near the extrema. GC-PINN captures the overall waveform more faithfully, although localized errors remain evident. ACR-PINN provides the most accurate slice-wise reconstruction, closely matching both the phase and amplitude of the reference solution, with consistently low pointwise errors across the entire spatial interval.

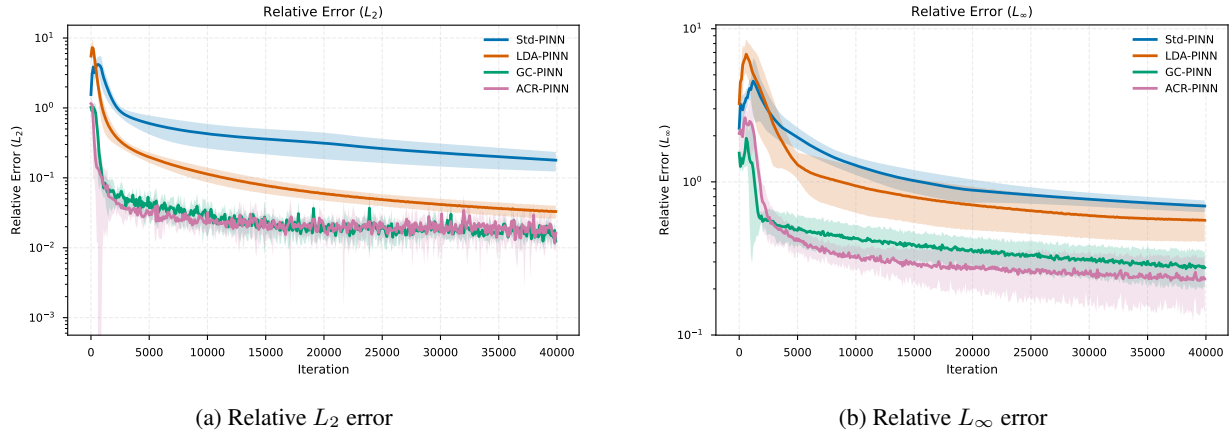


Figure 16: Comparison of relative L_2 and L_∞ errors for all models on the Helmholtz equation with $a_1 = 4$ and $a_2 = 4$.

The evolution of the relative L_2 and L_∞ errors during training, as shown in Fig. 16, reveals notable differences in convergence behavior. The standard PINN converges slowly and stagnates at a high error level, indicating difficulties in balancing competing physical constraints in the high-frequency regime. LDA-PINN exhibits faster error reduction during the early training stages but plateaus prematurely, suggesting that improved representation alone is insufficient to ensure stable convergence. Both GC-PINN and ACR-PINN display mild oscillations in the later training stages, which can be attributed to the selective activation of gradient projection when conflicts are detected. Despite these fluctuations, ACR-PINN consistently converges to the lowest error floor with reduced variance, demonstrating superior robustness and stability under severe oscillatory conditions.

Overall, this high-frequency experiment demonstrates that standard PINNs struggle when both representational and optimization challenges are intensified. While LDA and GC individually address complementary aspects of the problem,

their integration within ACR-PINN produces the most accurate, stable, and reliable performance, underscoring the necessity of architecture–optimization co-design for solving challenging oscillatory PDEs.

3.3 Klein–Gordon Equation

The Klein–Gordon equation is a prototypical nonlinear partial differential equation that arises in various physical contexts, including relativistic quantum mechanics, nonlinear optics, and solid-state physics [34]. It governs the evolution of scalar fields and is well known for exhibiting rich nonlinear wave phenomena, making it a challenging benchmark for physics-informed learning methods.

We consider the one-dimensional time-dependent Klein–Gordon initial–boundary value problem of the form

$$u_{tt}(x, t) + \alpha u_{xx}(x, t) + \beta u(x, t) + \gamma u^k(x, t) = f(x, t), \quad (x, t) \in \Omega \times [0, T], \quad (31)$$

subject to the initial conditions

$$u(x, 0) = g_1(x), \quad u_t(x, 0) = g_2(x), \quad x \in \Omega, \quad (32)$$

and the boundary condition

$$u(x, t) = h(x, t), \quad (x, t) \in \partial\Omega \times [0, T]. \quad (33)$$

Here, $u(x, t)$ denotes the unknown field, α , β , and γ are prescribed coefficients, and $k \in \mathbb{N}$ specifies the order of the nonlinear term. The functions $f(x, t)$, $g_1(x)$, $g_2(x)$, and $h(x, t)$ are assumed to be sufficiently smooth and mutually compatible.

In the present study, we focus on the following configuration:

$$\Omega = [0, 1], \quad T = 1, \quad \alpha = -1, \quad \beta = 0, \quad \gamma = 1, \quad k = 3. \quad (34)$$

To facilitate quantitative evaluation, a manufactured-solution setting is adopted. Specifically, the exact solution is prescribed as

$$u(x, t) = x \cos(5\pi t) + (xt)^3. \quad (35)$$

Substituting this expression into the governing equation yields the corresponding forcing term $f(x, t)$ in a consistent manner. The initial and boundary conditions are directly derived from the exact solution, namely,

$$g_1(x) = u(x, 0), \quad g_2(x) = u_t(x, 0), \quad h(x, t) = u(x, t)|_{\partial\Omega}. \quad (36)$$

This manufactured formulation enables precise error quantification and provides a controlled testbed for assessing the capability of PINN-based models to capture nonlinear, time-dependent dynamics under multiple competing physical constraints.

For the Klein–Gordon experiments, the training dataset consists of 200 initial-condition points, 200 boundary-condition points, and 10,000 interior collocation points generated using Latin Hypercube Sampling (LHS). Unless otherwise specified, all models employ an identical neural network architecture, comprising an input layer with two neurons corresponding to the spatial coordinate x and time t , followed by three hidden layers with 50 neurons each and \tanh activation functions, and a single output neuron representing the solution $u(x, t)$.

Table 4: Comparison of relative L_2 and L_∞ errors for the Klein–Gordon equation.

Model	Iterations	$\bar{\epsilon}_{L_2} \pm \sigma(\epsilon_{L_2})$	$\bar{\epsilon}_{L_\infty} \pm \sigma(\epsilon_{L_\infty})$
Std-PINN	40000	$6.23 \times 10^{-2} \pm 1.35 \times 10^{-2}$	$8.39 \times 10^{-2} \pm 2.71 \times 10^{-2}$
LDA-PINN	40000	$2.17 \times 10^{-2} \pm 4.05 \times 10^{-3}$	$3.69 \times 10^{-2} \pm 1.40 \times 10^{-2}$
GC-PINN	40000	$8.71 \times 10^{-3} \pm 1.79 \times 10^{-3}$	$2.29 \times 10^{-2} \pm 1.68 \times 10^{-3}$
ACR-PINN	40000	$3.33 \times 10^{-3} \pm 1.21 \times 10^{-3}$	$1.18 \times 10^{-2} \pm 6.90 \times 10^{-3}$

Table 4 summarizes the relative L_2 and L_∞ errors for the Klein–Gordon equation, averaged over five independent runs. The standard PINN performs the worst, with a relative L_2 error of 6.23×10^{-2} and a comparable L_∞ error of 8.39×10^{-2} . The consistently large errors, along with noticeable variance across runs, indicate that the baseline model struggles to reliably capture the nonlinear and time-dependent solution dynamics under heterogeneous constraints. Introducing the layer-wise dynamic attention mechanism leads to a clear improvement. LDA-PINN reduces the mean L_2 error to 2.17×10^{-2} (approximately a 65% reduction relative to Std-PINN) and decreases the L_∞ error to 3.69×10^{-2} , suggesting that re-encoding the physical input at each layer enhances representational flexibility and improves the approximation of localized features. Nevertheless, the remaining peak-wise error and its variance imply

that architectural enhancement alone does not fully eliminate optimization instability when multiple physical losses interact. GC-PINN exhibits markedly different behavior. By mitigating destructive gradient interference during training, GC-PINN further reduces the L_2 error to 8.71×10^{-3} , corresponding to an approximately $7.2 \times$ improvement over Std-PINN. This observation highlights that, for the Klein–Gordon problem, optimization conflicts among heterogeneous constraints constitute a major bottleneck beyond representational limitations. However, while the L_∞ error improves to 2.29×10^{-2} , it remains higher than the corresponding L_2 trend would suggest, indicating that gradient-conflict resolution alone may still leave residual local inaccuracies in challenging regions of the solution. Among all models, ACR-PINN consistently achieves the best overall performance. It attains the lowest mean errors in both norms (3.33×10^{-3} in L_2 and 1.18×10^{-2} in L_∞) and exhibits reduced variability across runs, reflecting improved robustness and reliability. These results confirm that for nonlinear, time-dependent Klein–Gordon dynamics, neither architectural refinement nor optimization improvement alone is sufficient to fully address the training difficulties. Instead, jointly enhancing representation learning via layer-wise attention and stabilizing optimization through conflict-aware gradient updates is essential for obtaining accurate and stable PINN solutions.

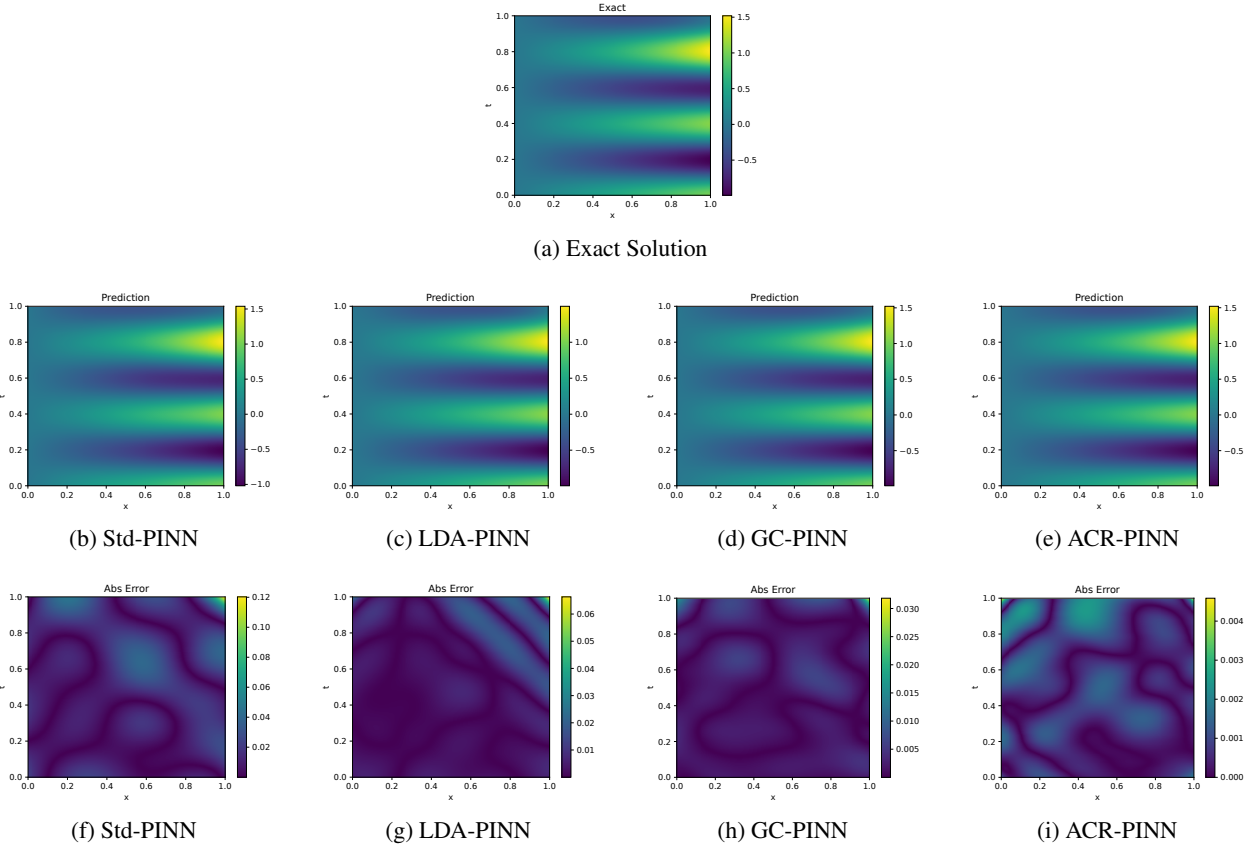


Figure 17: Visualization of the exact solution, predicted solutions, and absolute error distributions for the Klein–Gordon equation.

Figure 17 compares the exact solution, predicted solutions, and absolute error distributions for the Klein–Gordon equation. Unlike previous benchmarks dominated by spatial discontinuities or high-frequency oscillations, this problem emphasizes nonlinear spatio-temporal coupling and long-term temporal evolution. The standard PINN exhibits noticeable global deviations, with errors accumulating across the space–time domain. These deviations are not confined to isolated regions but reflect the challenge of maintaining temporal consistency under nonlinear dynamics. By introducing layer-wise dynamic attention, LDA-PINN improves the overall solution structure and reduces global error levels. However, localized error patterns remain visible, particularly in regions where nonlinear interactions intensify over time, indicating that representational enhancement alone is insufficient to fully control error propagation. GC-PINN further suppresses error growth by mitigating destructive gradient interactions among competing physical constraints. The resulting predictions are smoother and more temporally coherent, although residual discrepancies persist due to the limited expressiveness of the underlying MLP backbone. In contrast, ACR-PINN provides the closest match to the exact

solution. Its error distribution remains uniformly bounded throughout the space–time domain, demonstrating effective control of nonlinear error accumulation. This behavior highlights the complementary roles of attentive representation learning and conflict-resolved optimization in stabilizing nonlinear temporal dynamics.

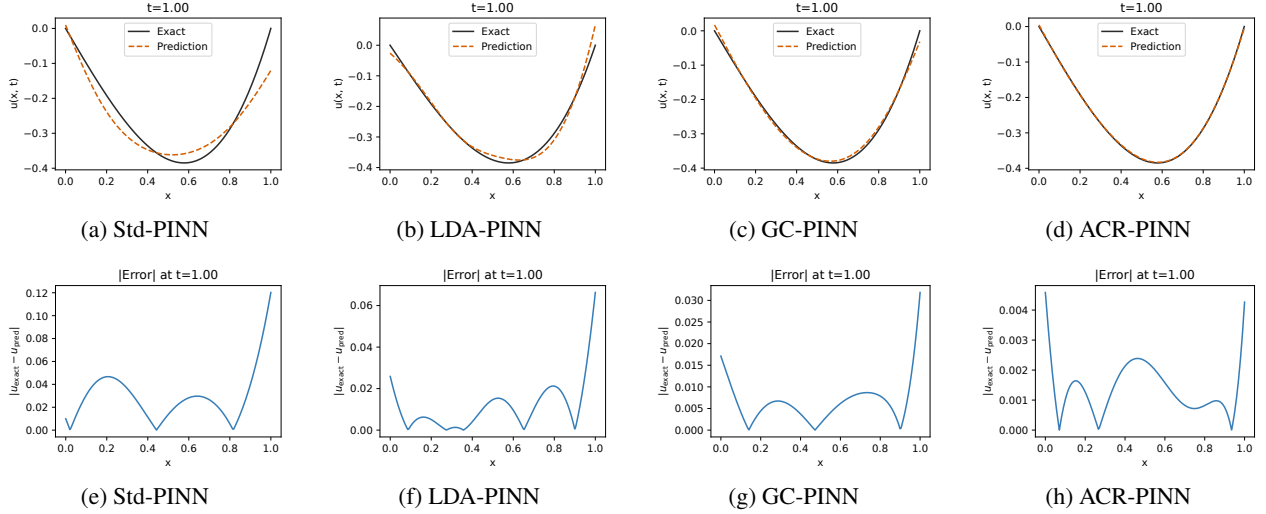


Figure 18: Time-slice comparison of predicted solutions and absolute errors for the Klein–Gordon equation at $t = 1.00$.

The time-slice comparison at $t=1.00$, shown in Fig. 18, further elucidates the differences among the models. The standard PINN fails to accurately follow the solution trajectory, exhibiting both amplitude distortions and temporal drift relative to the exact solution. LDA-PINN captures the overall trend more faithfully, but noticeable local discrepancies persist, particularly in regions affected by nonlinear growth. GC-PINN achieves improved trajectory tracking and reduces pointwise deviations, indicating enhanced temporal stability due to conflict-resolved gradient updates. ACR-PINN attains the closest agreement with the reference solution across the entire spatial domain. Its corresponding absolute error profile remains consistently low, demonstrating superior accuracy in preserving the nonlinear temporal evolution of the solution.

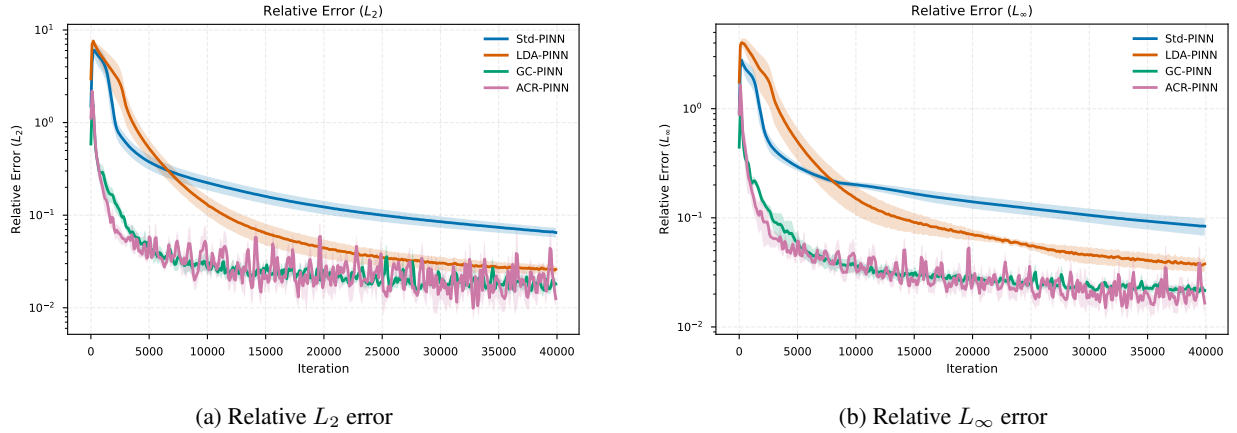


Figure 19: Comparison of relative L_2 and L_∞ errors for all models on the Klein–Gordon equation.

The evolution of the relative L_2 and L_∞ errors during training, shown in Fig. 19, reveals distinct convergence behaviors. The standard PINN converges slowly and saturates at a relatively high error level, reflecting limitations in both representational capacity and optimization dynamics for nonlinear, time-dependent problems. LDA-PINN achieves faster error reduction during the early training stages, benefiting from enhanced expressive power. However, its convergence gradually plateaus, suggesting that architectural improvements alone cannot fully resolve the optimization challenges caused by multiple competing constraints. GC-PINN exhibits more stable convergence by explicitly alleviating gradient conflicts, leading to a lower error floor and improved robustness compared to both Std-PINN

and LDA-PINN. ACR-PINN consistently converges to the lowest error levels across both metrics. Although mild oscillations appear in the later training stages, these fluctuations remain bounded and result from the conditional activation of gradient projection rather than numerical instability.

Overall, the Klein–Gordon experiments demonstrate that nonlinear, time-dependent PDEs impose simultaneous demands on representational fidelity and optimization stability. While attentive architectures and conflict-resolved optimization individually address complementary aspects of this challenge, their integration within ACR-PINN produces the most accurate, stable, and reliable performance.

3.4 Lid-Driven Cavity Flow

The lid-driven cavity flow, governed by the incompressible Navier–Stokes equations, is a classical benchmark problem in computational fluid dynamics and has been extensively studied as a reference case for incompressible viscous flows [14]. Its well-documented flow structures, including primary and secondary vortices, make it particularly suitable for evaluating the accuracy and stability of numerical solvers under incompressibility constraints. In this work, we consider the two-dimensional, steady-state lid-driven cavity flow on a unit square domain.

The governing equations are given by

$$\mathbf{u} \cdot \nabla \mathbf{u} + \nabla p - \frac{1}{Re} \Delta \mathbf{u} = \mathbf{0}, \quad \mathbf{x} \in \Omega, \quad (37)$$

$$\nabla \cdot \mathbf{u} = 0, \quad \mathbf{x} \in \Omega, \quad (38)$$

where $\mathbf{x} = (x, y) \in \Omega = [0, 1] \times [0, 1]$, $\mathbf{u} = (u, v)$ denotes the velocity field, p is the pressure field, and the Reynolds number is fixed at $Re = 100$.

The boundary conditions correspond to a uniformly moving lid at the top boundary and no-slip conditions on the remaining walls:

$$\mathbf{u}(\mathbf{x}) = (1, 0), \quad \mathbf{x} \in \Gamma_1, \quad (39)$$

$$\mathbf{u}(\mathbf{x}) = (0, 0), \quad \mathbf{x} \in \Gamma_0, \quad (40)$$

where Γ_1 denotes the top boundary and Γ_0 represents the other three stationary boundaries.

To enforce the incompressibility constraint in a physically consistent manner, we adopt a stream function formulation following [14]. Specifically, a scalar stream function $\psi(x, y)$ is introduced such that the velocity field is expressed as

$$u = \frac{\partial \psi}{\partial y}, \quad v = -\frac{\partial \psi}{\partial x}. \quad (41)$$

This formulation inherently satisfies the divergence-free condition (38), eliminating the need for additional penalty terms. Consequently, the PINN is trained to predict the stream function $\psi(x, y)$ together with the pressure field $p(x, y)$.

Reference solutions for the velocity field are obtained from high-fidelity finite difference simulations reported in [14], which serve as the ground truth for quantitative evaluation.

For training, 1,000 interior collocation points are sampled within the domain using Latin Hypercube Sampling. Along the boundaries, 300 points are sampled on the moving lid Γ_1 , while 100 points are sampled on each of the remaining stationary boundaries. This non-uniform boundary sampling reflects the dominant influence of the moving lid on the flow dynamics.

All models share the same neural network architecture, consisting of an input layer with two neurons corresponding to the spatial coordinates (x, y) , three hidden layers with 50 neurons each using \tanh activation functions, and an output layer with two neurons representing the stream function $\psi(x, y)$ and the pressure field $p(x, y)$.

Table 5: Comparison of relative L_2 and L_∞ errors for the lid-driven cavity flow.

Model	Iterations	$\bar{\varepsilon}_{L_2} \pm \sigma(\varepsilon_{L_2})$	$\bar{\varepsilon}_{L_\infty} \pm \sigma(\varepsilon_{L_\infty})$
Std-PINN	20000	$1.34 \times 10^{-1} \pm 2.75 \times 10^{-2}$	$6.76 \times 10^{-1} \pm 5.58 \times 10^{-2}$
LDA-PINN	20000	$5.59 \times 10^{-2} \pm 1.98 \times 10^{-2}$	$4.57 \times 10^{-1} \pm 9.73 \times 10^{-2}$
GC-PINN	20000	$9.00 \times 10^{-2} \pm 1.55 \times 10^{-2}$	$5.44 \times 10^{-1} \pm 6.78 \times 10^{-2}$
ACR-PINN	20000	$4.37 \times 10^{-2} \pm 1.80 \times 10^{-2}$	$3.02 \times 10^{-1} \pm 9.85 \times 10^{-2}$

Table 5 summarizes the relative L_2 and L_∞ errors obtained by the compared models for the lid-driven cavity flow at $Re = 100$. Overall, all enhanced PINN variants outperform the standard PINN, indicating that both architectural

and optimization-level improvements contribute positively to this strongly constrained incompressible flow problem. The standard PINN yields the largest errors in both norms, with a relative L_2 error on the order of 10^{-1} and a comparatively large L_∞ error. This behavior reflects the intrinsic difficulty of simultaneously enforcing the nonlinear momentum equations and the incompressibility constraint under heterogeneous boundary conditions, particularly in regions dominated by near-wall shear and vortex formation. Introducing the layer-wise dynamic attention mechanism leads to a clear improvement in predictive accuracy. LDA-PINN reduces the relative L_2 error by more than a factor of two compared with the standard PINN, indicating an enhanced capability to represent the complex flow structures induced by the moving lid. Nevertheless, the remaining L_∞ error suggests that resolving local extrema and near-wall features remains challenging when architectural enhancement is applied alone. GC-PINN achieves moderate accuracy gains over the baseline model. While conflict-resolved gradient optimization improves training stability and mitigates interference among competing physical constraints, its impact on overall accuracy is limited by the representational capacity of the underlying MLP architecture. As a result, the error reduction achieved by GC-PINN is less pronounced than that of LDA-PINN in this setting. The proposed ACR-PINN delivers the best overall performance. It attains the lowest errors in both L_2 and L_∞ norms, reducing the relative L_2 error to below 5×10^{-2} while substantially suppressing worst-case local deviations. These results demonstrate that combining attentive representation learning with conflict-resolved optimization is particularly effective for incompressible flow problems, where nonlinear coupling, boundary-driven dynamics, and strict physical constraints must be satisfied simultaneously.

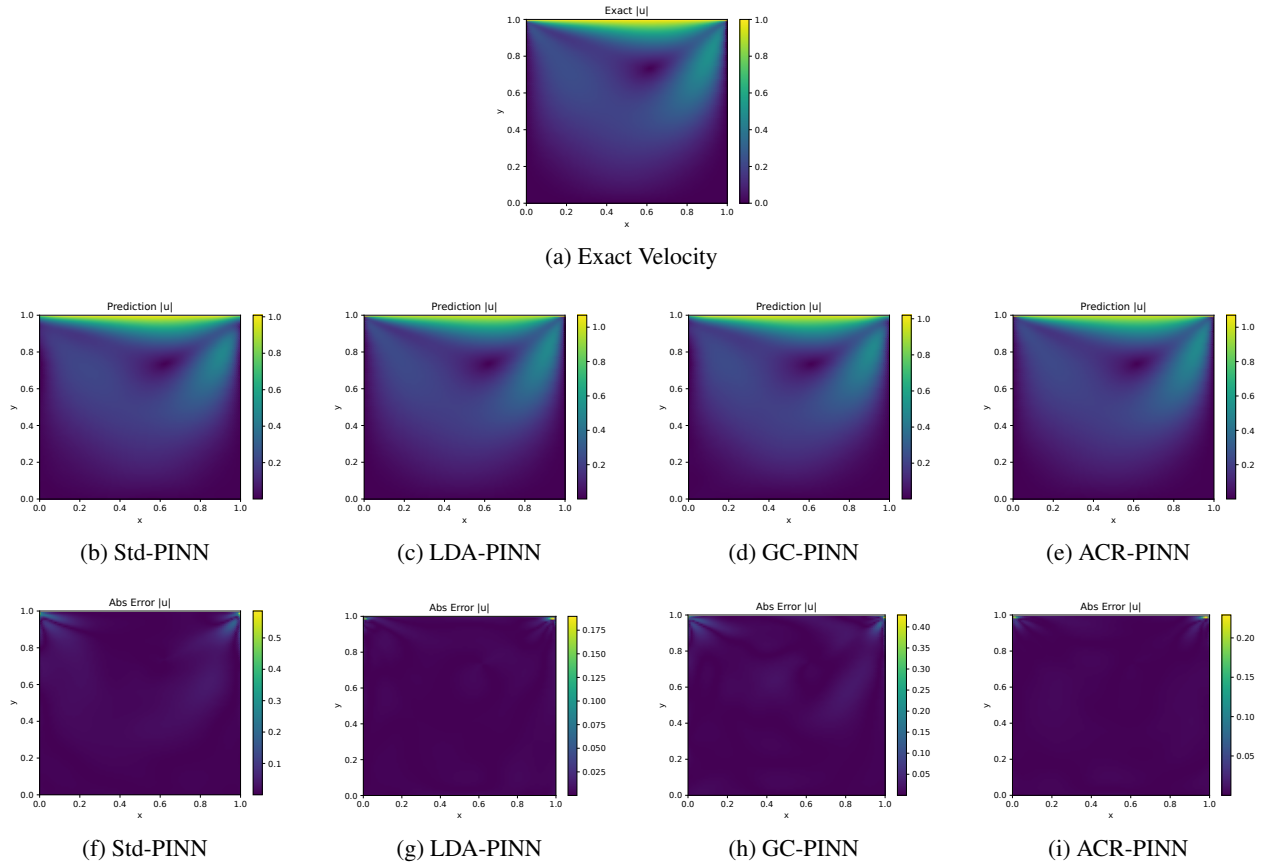


Figure 20: Visualization of the exact velocity field, predicted velocity fields, and velocity error distributions for the lid-driven cavity flow.

Figure 20 presents the reference velocity magnitude, the predicted velocity fields obtained by various models, and the corresponding absolute error distributions. The standard PINN reproduces the large-scale circulation pattern of the cavity flow; however, noticeable discrepancies appear in regions dominated by strong shear and rapid spatial variation. In particular, near the moving lid and the upper corners, the predicted velocity exhibits visible distortions, resulting in pronounced localized errors. In contrast, LDA-PINN yields a substantially improved velocity field. The error magnitude is markedly reduced, especially in near-wall regions where sharp gradients are present. This improvement indicates that the layer-wise reinterpretation of input coordinates enhances the network's ability to represent boundary-driven

flow features and localized shear layers. GC-PINN also reduces the overall error compared with the standard PINN, reflecting the benefit of alleviating destructive gradient interactions among the momentum equations and boundary constraints. However, residual discrepancies persist in regions that demand higher representational fidelity, suggesting that optimization-level conflict mitigation alone is insufficient when the backbone architecture remains limited. Among all methods, ACR-PINN provides the closest agreement with the reference solution. Its error distribution is uniformly suppressed across the domain, with no evident high-error concentrations near the lid or cavity corners. This result highlights the complementary effects of attentive representation learning and conflict-resolved optimization in capturing the coupled, boundary-dominated dynamics of incompressible cavity flow.

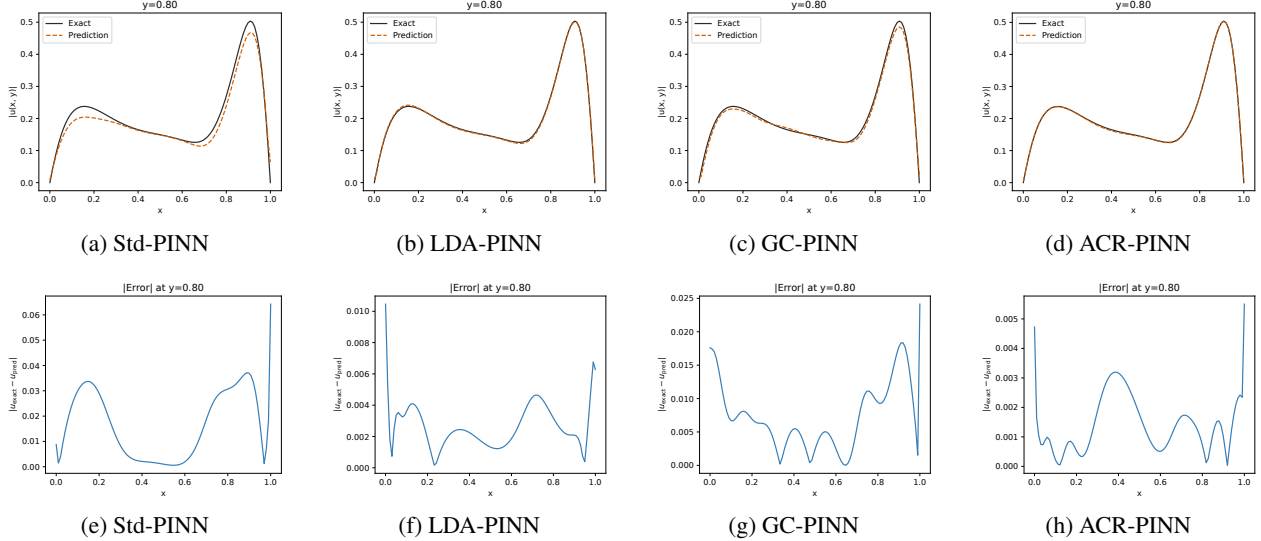


Figure 21: Spatial slice comparison of predicted solutions and absolute errors for the lid-driven cavity flow at $y = 0.80$.

To further assess local accuracy in the region most strongly influenced by the moving lid, Fig. 21 compares the predicted velocity profiles and absolute errors along the horizontal slice at $y = 0.80$. The standard PINN exhibits clear amplitude mismatches around the velocity peak, resulting in large pointwise errors near the shear-dominated region. LDA-PINN significantly improves both amplitude and phase alignment with the reference profile. The corresponding error curve is smoother and substantially reduced, indicating enhanced resolution of near-wall velocity gradients. GC-PINN preserves the overall waveform more faithfully than the standard PINN; however, noticeable deviations remain near the extrema, suggesting that gradient conflict mitigation alone cannot fully compensate for the limited expressiveness of a conventional MLP backbone. In contrast, ACR-PINN achieves excellent agreement with the reference solution across the entire slice. Its pointwise error remains consistently low, demonstrating superior local accuracy in regions where strong velocity gradients and competing physical constraints coexist.

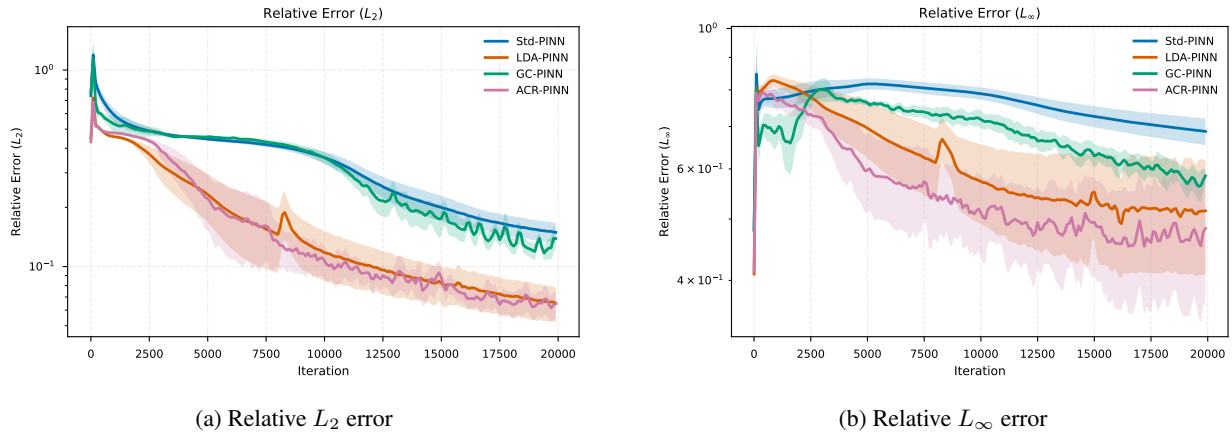


Figure 22: Comparison of relative L_2 and L_∞ errors for all models for the lid-driven cavity flow.

The evolution of the relative L_2 and L_∞ errors during training is shown in Fig. 22. The standard PINN converges slowly and stagnates at comparatively high error levels in both metrics, reflecting limitations in representation and optimization when applied to constraint-dominated incompressible flows. LDA-PINN exhibits faster and more consistent error reduction due to its enhanced representational flexibility. Nevertheless, its improvement in the L_∞ norm is less pronounced, indicating that local inaccuracies near sharp gradients and walls are not fully resolved by architectural enhancements alone. GC-PINN displays smoother training dynamics by suppressing destructive gradient interference, yet its final accuracy remains constrained by the expressiveness of the underlying MLP architecture. ACR-PINN consistently converges to the lowest error floor in both norms, with a particularly notable advantage in the L_∞ metric. This indicates more effective control of worst-case errors, which are typically associated with near-wall regions and strong shear layers in lid-driven cavity flows.

Mild oscillations are observed during the later stages of training for both GC-PINN and ACR-PINN. These fluctuations result from the conditional nature of gradient projection, which is activated only when conflicts among physical constraints are detected, leading to piecewise-defined update directions. This behavior is algorithmic rather than pathological and remains well bounded throughout training. Importantly, these oscillations do not compromise the worst-case accuracy. On the contrary, ACR-PINN achieves the lowest final L_∞ error, indicating that conflict-resolved optimization effectively suppresses extreme local deviations despite the non-smooth update trajectories.

Overall, the lid-driven cavity experiments reinforce the conclusions drawn from earlier benchmarks while highlighting problem-specific characteristics. LDA primarily enhances the representation of complex, boundary-induced flow structures; GC improves optimization stability under competing physical constraints; and their integration in ACR-PINN yields superior control of both global and local errors. This makes ACR-PINN particularly well-suited for nonlinear, coupled, and boundary-driven incompressible flow problems where L_∞ accuracy is critically important.

4 Conclusion

In this work, we investigated the training challenges of PINNs from a unified architecture–optimization perspective and proposed a co-design framework to systematically address these issues. Rather than treating network representation and optimization dynamics as independent components, the proposed framework explicitly considers their interaction through gradient flow during training.

From an architectural perspective, we introduced a layer-wise dynamic attention mechanism that enables input-conditioned reinterpretation at each hidden layer, resulting in the LDA-PINN model with enhanced representational flexibility. From an optimization standpoint, we reformulated PINN training as a multi-task learning problem and analyzed gradient conflicts arising from heterogeneous physical constraints. Based on this analysis, we incorporated conflict-resolved gradient updates and developed GC-PINN to suppress destructive gradient interference without altering the original loss formulation. By integrating these two complementary components, we further proposed ACR-PINN, which combines attentive representations with conflict-resolved optimization in a unified and lightweight framework.

Extensive numerical experiments on a variety of representative PDE benchmarks—including nonlinear, oscillatory, time-dependent, and coupled flow problems—demonstrate the effectiveness of the proposed approach. Across all test cases, LDA-PINN and GC-PINN consistently outperform the standard PINN by addressing representational and optimization bottlenecks from different perspectives. More importantly, the co-designed ACR-PINN achieves the best overall performance, delivering substantial improvements in both relative L_2 and L_∞ accuracy and typically reducing errors by at least one order of magnitude compared to the baseline PINN. These results confirm that jointly designing network architecture and gradient interaction mechanisms is crucial for robust and accurate PINN training.

Several avenues remain open for future research. First, projection-based conflict resolution introduces piecewise-defined update directions, which may cause mild oscillations during training when gradient conflicts occur frequently. Developing smoother or adaptive conflict-handling strategies—such as conflict-aware schedules or soft projection mechanisms—could further enhance optimization stability. Second, although this study focuses on canonical PDE benchmarks, extending the proposed framework to strongly coupled multi-physics systems—such as thermo-fluid, magnetohydrodynamic, or fluid–structure interaction problems—warrants further investigation, as constraint heterogeneity and cross-field interactions are more pronounced in these contexts. Finally, scaling the framework to high-dimensional and large-scale PDE problems remains a significant challenge, necessitating advances in scalable architectures, efficient sampling strategies, and memory-aware training schemes.

Funding information

The authors gratefully acknowledge the support from the National Natural Science Foundation of China (No. 12371434), the National Key R&D Program of China (No. 2022YFE03040002), the Foundation of the Sichuan Provincial Department of Science and Technology (No. 2026NSFSC0138), the Key Laboratory of Numerical Simulation of Sichuan Provincial Universities (Nos. KLNS-2023SZFZ002 and KLNS-2023SZFZ005), and the Key Laboratory of Mathematical Meteorology (No. 2025Z0340).

Declaration of Competing Interest

The authors declare that they have no known competing financial interests or personal relationships that could have appeared to influence the work reported in this paper.

Data Availability

The data supporting the findings of this study are available from the corresponding author upon reasonable request. The code used to generate the results is publicly available at <https://github.com/PanChengN/ACR-PINN>.

References

- [1] Maziar Raissi, Paris Perdikaris, and George E Karniadakis. Physics-informed neural networks: A deep learning framework for solving forward and inverse problems involving nonlinear partial differential equations. *Journal of Computational physics*, 378:686–707, 2019.
- [2] George Em Karniadakis, Ioannis G Kevrekidis, Lu Lu, Paris Perdikaris, Sifan Wang, and Liu Yang. Physics-informed machine learning. *Nature Reviews Physics*, 3(6):422–440, 2021.
- [3] Atilim Gunes Baydin, Barak A Pearlmutter, Alexey Andreyevich Radul, and Jeffrey Mark Siskind. Automatic differentiation in machine learning: a survey. *Journal of machine learning research*, 18(153):1–43, 2018.
- [4] Aditi Krishnapriyan, Amir Gholami, Shandian Zhe, Robert Kirby, and Michael W Mahoney. Characterizing possible failure modes in physics-informed neural networks. *Advances in neural information processing systems*, 34:26548–26560, 2021.
- [5] Xiaowei Jin, Shengze Cai, Hui Li, and George Em Karniadakis. Nsfnets (navier-stokes flow nets): Physics-informed neural networks for the incompressible navier-stokes equations. *Journal of Computational Physics*, 426:109951, 2021.
- [6] Ameya D Jagtap, Zhiping Mao, Nikolaus Adams, and George Em Karniadakis. Physics-informed neural networks for inverse problems in supersonic flows. *Journal of Computational Physics*, 466:111402, 2022.
- [7] Shengze Cai, Zhicheng Wang, Sifan Wang, Paris Perdikaris, and George Em Karniadakis. Physics-informed neural networks for heat transfer problems. *Journal of Heat Transfer*, 143(6):060801, 2021.
- [8] Jiaxuan Xu, Han Wei, and Hua Bao. Physics-informed neural networks for studying heat transfer in porous media. *International Journal of Heat and Mass Transfer*, 217:124671, 2023.
- [9] Ehsan Haghhighat, Maziar Raissi, Adrian Moure, Hector Gomez, and Ruben Juanes. A physics-informed deep learning framework for inversion and surrogate modeling in solid mechanics. *Computer Methods in Applied Mechanics and Engineering*, 379:113741, 2021.
- [10] Haoteng Hu, Lehua Qi, and Xujiang Chao. Physics-informed neural networks (pinn) for computational solid mechanics: Numerical frameworks and applications. *Thin-Walled Structures*, 205:112495, 2024.
- [11] Majid Rasht-Behesht, Christian Huber, Khemraj Shukla, and George Em Karniadakis. Physics-informed neural networks (pinns) for wave propagation and full waveform inversions. *Journal of Geophysical Research: Solid Earth*, 127(5):e2021JB023120, 2022.
- [12] Shaikhah Alkhadhr and Mohamed Almekkawy. Wave equation modeling via physics-informed neural networks: Models of soft and hard constraints for initial and boundary conditions. *Sensors*, 23(5):2792, 2023.
- [13] Lin Chen, Ben Li, Chenyi Luo, and Xiaoming Lei. Wavenets: physics-informed neural networks for full-field recovery of rotational flow beneath large-amplitude periodic water waves. *Engineering with Computers*, 40(5):2819–2839, 2024.

- [14] Sifan Wang, Yujun Teng, and Paris Perdikaris. Understanding and mitigating gradient flow pathologies in physics-informed neural networks. *SIAM Journal on Scientific Computing*, 43(5):A3055–A3081, 2021.
- [15] Sifan Wang, Xinling Yu, and Paris Perdikaris. When and why pinns fail to train: A neural tangent kernel perspective. *Journal of Computational Physics*, 449:110768, 2022.
- [16] Jorge F Urbán, Petros Stefanou, and José A Pons. Unveiling the optimization process of physics informed neural networks: How accurate and competitive can pinns be? *Journal of Computational Physics*, 523:113656, 2025.
- [17] Yong Wang, Yanzhong Yao, Jiawei Guo, and Zhiming Gao. A practical pinn framework for multi-scale problems with multi-magnitude loss terms. *Journal of Computational Physics*, 510:113112, 2024.
- [18] Kuang Luo, Jingshang Zhao, Yingping Wang, Jiayao Li, Junjie Wen, Jiong Liang, Henry Soekmadji, and Shaolin Liao. Physics-informed neural networks for pde problems: a comprehensive review. *Artificial Intelligence Review*, 58(10):323, 2025.
- [19] Suryanarayana Maddu, Dominik Sturm, Christian L Müller, and Ivo F Sbalzarini. Inverse dirichlet weighting enables reliable training of physics informed neural networks. *Machine Learning: Science and Technology*, 3(1):015026, 2022.
- [20] Shota Deguchi and Mitsuteru Asai. Dynamic & norm-based weights to normalize imbalance in back-propagated gradients of physics-informed neural networks. *Journal of Physics Communications*, 7(7):075005, 2023.
- [21] Pancheng Niu, Jun Guo, Yongming Chen, Yuqian Zhou, Minfu Feng, and Yanchao Shi. Improved physics-informed neural network in mitigating gradient-related failures. *Neurocomputing*, 638:130167, 2025.
- [22] Tianhe Yu, Saurabh Kumar, Abhishek Gupta, Sergey Levine, Karol Hausman, and Chelsea Finn. Gradient surgery for multi-task learning. *Advances in neural information processing systems*, 33:5824–5836, 2020.
- [23] Jeremy Yu, Lu Lu, Xuhui Meng, and George Em Karniadakis. Gradient-enhanced physics-informed neural networks for forward and inverse pde problems. *Computer Methods in Applied Mechanics and Engineering*, 393:114823, 2022.
- [24] Dehao Liu and Yan Wang. A dual-dimer method for training physics-constrained neural networks with minimax architecture. *Neural Networks*, 136:112–125, 2021.
- [25] Yanjie Song, He Wang, He Yang, Maria Luisa Taccari, and Xiaohui Chen. Loss-attentional physics-informed neural networks. *Journal of Computational Physics*, 501:112781, 2024.
- [26] Ameya D Jagtap, Kenji Kawaguchi, and George Em Karniadakis. Adaptive activation functions accelerate convergence in deep and physics-informed neural networks. *Journal of Computational Physics*, 404:109136, 2020.
- [27] Matthew Tancik, Pratul Srinivasan, Ben Mildenhall, Sara Fridovich-Keil, Nithin Raghavan, Utkarsh Singhal, Ravi Ramamoorthi, Jonathan Barron, and Ren Ng. Fourier features let networks learn high frequency functions in low dimensional domains. *Advances in neural information processing systems*, 33:7537–7547, 2020.
- [28] Ziming Liu, Yixuan Wang, Sachin Vaidya, Fabian Ruehle, James Halverson, Marin Soljačić, Thomas Y Hou, and Max Tegmark. Kan: Kolmogorov-arnold networks. *arXiv preprint arXiv:2404.19756*, 2024.
- [29] Bo Liu, Xingchao Liu, Xiaojie Jin, Peter Stone, and Qiang Liu. Conflict-averse gradient descent for multi-task learning. *Advances in Neural Information Processing Systems*, 34:18878–18890, 2021.
- [30] Kurt Hornik, Maxwell Stinchcombe, and Halbert White. Multilayer feedforward networks are universal approximators. *Neural networks*, 2(5):359–366, 1989.
- [31] Ashish Vaswani, Noam Shazeer, Niki Parmar, Jakob Uszkoreit, Llion Jones, Aidan N Gomez, Łukasz Kaiser, and Illia Polosukhin. Attention is all you need. *Advances in neural information processing systems*, 30, 2017.
- [32] Johannes Martinus Burgers. *The nonlinear diffusion equation: asymptotic solutions and statistical problems*. Springer Science & Business Media, 2013.
- [33] David L Colton, Rainer Kress, and Rainer Kress. *Inverse acoustic and electromagnetic scattering theory*, volume 93. Springer, 1998.
- [34] Abdul-Majid Wazwaz. New travelling wave solutions to the boussinesq and the klein–gordon equations. *Communications in Nonlinear Science and Numerical Simulation*, 13(5):889–901, 2008.